

AFRL-SR-AR-TR-03-

REPORT DOCUMENTATION PAGE

0274

Public reporting burden for this collection of information is estimated to average 1 hour per response, including the time for reviewing the data needed, and completing and reviewing this collection of information. Send comments regarding this burden estimate or any reducing this burden to Washington Headquarters Services, Directorate for Information Operations and Reports, 1215 Jefferson Day Management and Budget, Paperwork Reduction Project (0704-0188), Washington, DC 20503

1. AGENCY USE ONLY (Leave blank)		2. REPORT DATE June 24, 2003		3. REPORT TYPE AND DATES COVERED FINAL REPORT August 1988-March 2002	
4. TITLE AND SUBTITLE AN EXTREMELY SENSITIVE PZT-BASED MEMS MAGNETOMETER FOR USE AS AN ORIENTATION SENSOR				5. FUNDING NUMBERS AFOSR GRANT: F49620-98-1-0500	
6. AUTHOR(S) Dennis K. Wickenden					
7. PERFORMING ORGANIZATION NAME(S) AND ADDRESS(ES) Johns Hopkins University Applied Physics Laboratory 11100 Johns Hopkins Road Laurel, MD 20723				8. PERFORMING ORGANIZATION REPORT NUMBER RSS-03-170	
9. SPONSORING / MONITORING AGENCY NAME(S) AND ADDRESS(ES) AFOSR/NA 4015 Wilson Boulevard Arlington, VA 22203				10. SPONSORING / MONITORING AGENCY REPORT NUMBER	
11. SUPPLEMENTARY NOTES					
12a. DISTRIBUTION / AVAILABILITY STATEMENT Approved for public release; distribution unlimited.				12b. DISTRIBUTION CODE	
13. ABSTRACT (Maximum 200 Words) The objective of this project was to develop a sensitive MEMS-based magnetometer for use as an orientation sensor on spinning projectiles. The magnetometer was derived from the JHU/APL resonating xylophone bar with sensitivity linearly proportional to the drive current, mechanical Q at resonance, and the magnetic field. Polysilicon magnetometers demonstrated the size effects expected for such devices. Their sensitivity was limited by the relatively high sheet resistivity that restricted the drive current. A custom designed capacitive sense chip was developed and tested. PZT-based magnetometers (processed at ARL, Adelphi) were shown, at the current state of development, to be unsuitable for this application because of low Q's, asymmetric conducting layers, and high residual stress levels. The most promising technology appears to be based on CMOS-MEMS, although more development is required to produce practical devices. Even more recent advances in silicon-on-sapphire (SOS) technologies may make it possible to replace standard capacitive transduction schemes with much more sensitive optical ones. Studies have shown that a MEMS-based magnetometer would have important applications in addition to orientation sensing.					
14. SUBJECT TERMS MEMS, magnetometer, polysilicon, PZT				15. NUMBER OF PAGES 52	
				16. PRICE CODE	
17. SECURITY CLASSIFICATION OF REPORT UNCLASSIFIED	18. SECURITY CLASSIFICATION OF THIS PAGE UNCLASSIFIED	19. SECURITY CLASSIFICATION OF ABSTRACT UNCLASSIFIED	20. LIMITATION OF ABSTRACT		

NSN 7540-01-280-5500

Standard Form 298 (Rev. 2-89)
Prescribed by ANSI Std. Z39-18
298-102

20030731 060



JHU/APL
RSS-03-170
June 2003

An Extremely Sensitive PZT-based MEMS Magnetometer for Use as an Orientation Sensor

FINAL REPORT

Contract Number: AFOSR F49620-98-1-0500

Contract Period: August 1998 – March 2002

Principal Investigator:

Dennis K. Wickenden
The Johns Hopkins University
Applied Physics Laboratory
11100 Johns Hopkins Road
Laurel, MD 20723

Telephone: (240) 228 6249
E-mail: Dennis.Wickenden@jhuapl.edu

Contributors:

John Champion – JHU/APL
Eli Richards – JHU/APL
John Tucker – JHU/APL
Danielle Wesolek – JHU/APL
Brad Davis: ARL/WMRD, Aberdeen, MD
Madan Dubey: ARL/SEDD, Adelphi, MD

Submitted to:

AFOSR/NA
4015 Wilson Blvd., Rm 713
Arlington, VA 22203-1954

1. INTRODUCTION

Most inertial navigation systems in missile and projectile applications use an integrated approach that combines, for example, location data derived from GPS and orientation and acceleration data derived from onboard sensors. To date, the use of magnetometers to assist with the determination of a projectile's motion or heading has been severely limited. Two obvious reasons are: low sensitivity of standard compasses and proximity to ferrous objects that modify the strength and direction of the earth's magnetic field. However, this is not the case for free flight and orbital applications. For example, ARL(Aberdeen) has recently utilized a non-MEMS magnetometer to measure the spin of artillery projectiles in free flight [1]. Previously such data had been collected using an optically-based yawsonde that measures angles with respect to the sun [2]. The magnetometer sensor utilized a bridge circuit comprised of giant magnetoresistive (GMR) elements. When the bridge (two GMRs shielded and two unshielded) sweeps past a field line, a sinusoidal output is generated. The duty cycle is related to the spin rate of the object, but sensor output and conditioning electronics are limited to spin rates above 50 Hz. It was noted during these flight tests that amplitude modulations of the GMR signal were correlated with the yawsonde solar angle data. Further analysis has shown that with greater sensitivity and the efficient placement of multiple sensors at different orientations on the same device, the feasibility of high accuracy roll attitude and angular orientation measurement is extremely high [3]. A multiple sensor device is needed to avoid nulls that will occur when the sensitive axis aligns with magnetic field lines. This multi-sensor requirement leads naturally to the necessity of miniaturization and MEMS-based implementation. Furthermore, a sensor that directly measures angles will be significantly more accurate compared to angular rate sensors that are presently used for many inertial measurement applications. The accumulated errors (over long flight paths) of the current angular rate sensors yield position and attitude estimates that are often very crude and that rapidly degrade with time.

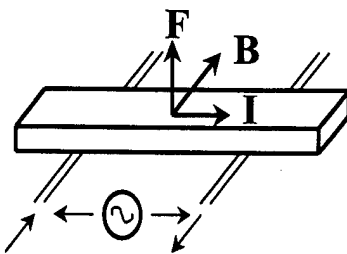


Fig 1. Principle of operation of xylophone bar magnetometer

Before the start of the project, JHU/APL had developed a novel magnetometer, based on a classical resonating xylophone bar, that was intrinsically linear and had a wide dynamic range such that it could measure magnetic field strengths from less than nanoteslas to Teslas [4]. Furthermore, it was ideally suited to miniaturization using a variety of MEMS-based technologies. This should result in magnetometer arrays with

miniature sensor elements, highly integrated electronics, inexpensive cost, and well suited to meet the intended application. The resonating xylophone bar magnetometer uses the Lorentz force as a measure of the magnetic field vector. It offers the potential of being light-weight and operating in a low power mode. True to its name, the device is based on a classical resonating xylophone bar. The principle of operation is shown in figure 1. The active element is a conductive bar supported at the nodes of its fundamental mode, of frequency f_0 , of mechanical vibration. An alternating sinusoidal current $[I \cos(2\pi ft)]$ is fed along the bar through the supports. In the absence of a magnetic field the bar will remain stationary.

In the presence of a magnetic field, B , the Lorentz force F , normal to the bar and the drive current, is given by:

$$F = I \times B \cos(2\pi ft) \quad (1)$$

This force causes the xylophone bar to vibrate, with a displacement, d , at the mid-point of the bar being given by:

$$d = \frac{d_{dc}}{\sqrt{\left[1 - \left(\frac{f}{f_0}\right)^2\right]^2 + \left(\frac{f}{Qf_0}\right)^2}} \quad (2)$$

The static deflection of a beam simply supported at both ends due to the Lorentz force uniformly distributed along its length is given by [5]:

$$d_{dc} = \frac{5Fl_2^4}{384EI_B} \quad (3)$$

where $I_B = ab^3/12$.

The phase angle between the driving current and the deflection is given by:

$$\phi = \arctan\left(\frac{f \cdot f_0}{Q(f_0^2 - f^2)}\right) \quad (4)$$

In the case of a free-free bar, where the effect of the supports can be neglected, the resonance frequency of the fundamental mode of the bar is given by:

$$f_0 = \frac{22.4}{2\pi} \sqrt{\frac{EI_B}{\rho w l^4}} \quad (5)$$

It can be seen from these equations that at resonance ($f = f_0$), the deflection of the xylophone bar is linearly proportional to the amplitude of the drive current, I , the

mechanical Q of the structure, and the magnetic flux density, B . Furthermore, since the xylophone bar includes no magnetic material, the sensor does not saturate in the presence of large magnetic fluxes. This results in a magnetometer with an extremely wide linear dynamic range. Macro-devices, chemically milled form Cu-Be foils, with dimensions of 5 mm x 0.5 mm x 0.025 mm, Q factors in the range 1000 - 5000, and drive currents of the order of one amp, have demonstrated dynamic ranges in excess of 80 dB with noise floors below 0.1 nT/ $\sqrt{\text{Hz}}$ [6].

Two approaches to implementing the MEMS-based xylophone magnetometer were pursued on this project. The first used polysilicon devices fabricated on the DARPA supported Standard Multi-User MEMS Processes (MUMPs) foundry service. The sensitivity of these devices was predicted to be limited by the current carrying capacity of the polysilicon. Therefore, the second approach was based on replacing the polysilicon with a platinum/lead zirconate titanate/platinum (Pt/PZT/Pt) sandwich structure for the xylophone bar. The PZT material deposition and processing was undertaken at ARL, Adelphi. Shock testing was undertaken at ARL, Aberdeen.

2. POLYSILICON MAGNETOMETER DESIGN AND CHARACTERIZATION

Throughout the course of the contract several designs of the polysilicon vibrating bar magnetometer were fabricated using the 3-layer foundry service at JDS Uniphase (ex MCNC and Cronos). Each design was divided into 4 quadrants, with each quadrant containing different series of layouts. Where possible (i.e. vibrating bars containing poly1) the bars had small dimples placed in the center and near the ends to alleviate stiction problems. The support electrodes are anchored either to the poly0 or silicon nitride using a "5 of diamonds" pattern to minimize the loss of vibrational energy. [7]

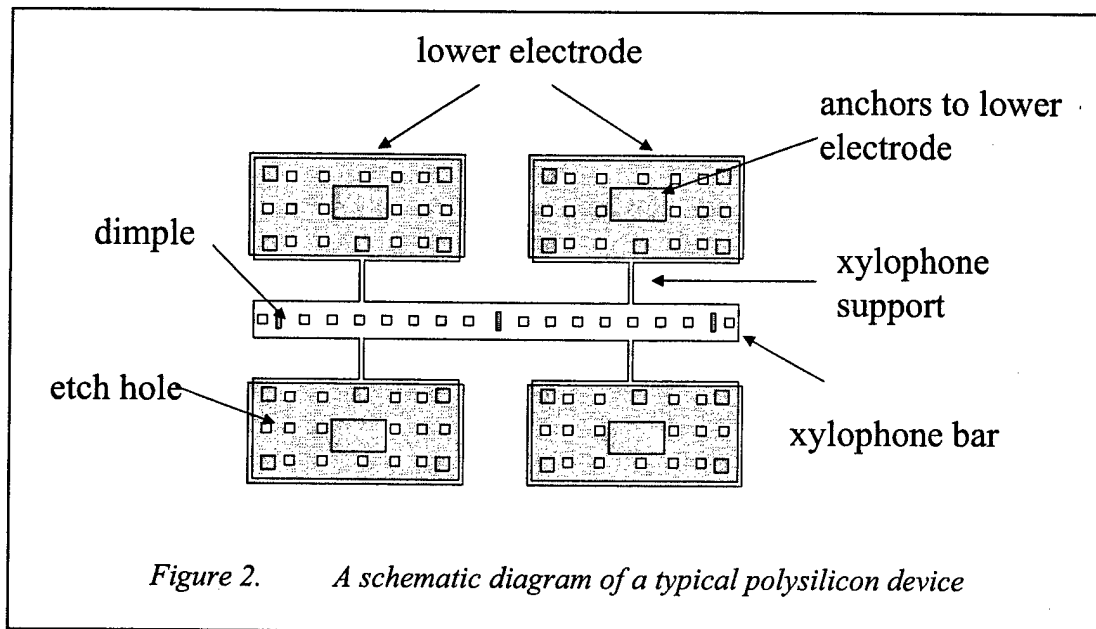


Figure 2. A schematic diagram of a typical polysilicon device

A schematic diagram of a typical poly1 device is shown in figure 2. The lower electrode consists of a 0.5 μm thick poly0 layer patterned on the silicon nitride-coated silicon substrate. The xylophone bar, support electrodes, and mounting pads are fabricated from 2 μm thick poly1 suspended (after release of the sacrificial silicon dioxide) 2 μm above the nitride layer or lower electrode. The mounting pads are attached to the lower electrode by the indicated patterns to provide a rigid anchor which minimizes vibrational coupling with the xylophone bar. Contact between the xylophone bar and the nitride layer is minimized by having 0.75 μm deep "dimples" in the center and toward the ends of the xylophone bar. An SEM micrograph of a released and mounted 500 x 50 x 2 μm xylophone bar is presented in figure 3. The micrograph clearly displays the anchor pattern, the etch holes, and the topographical evidence of the dimples. It also demonstrates the clean release of the xylophone structure.

Evaluation was carried out in a purpose-built evacuated chamber, using a bench-top beam deflection microscope. The beam of a laser diode is directed through a lens onto a node position on the xylophone bar in a way that the reflected beam is focused on the position sensitive detector (PSD). In this arrangement, the PSD is sensitive primarily

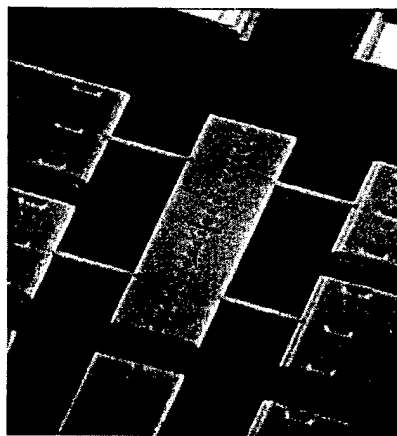


Figure 3. An SEM micrograph of a released and mounted $500 \times 50 \times 2 \mu\text{m}$ xylophone bar

to rotation of the beam at the node and not to vertical displacement. With the optical lever of 26 cm, the achieved sensitivity was of the order of $\Delta R/R=0.06/\text{mrad}$ or $\Delta R=0.3\text{V/mrad}$, where a typical $R=5\text{V}$ is the amplifier sum output for the reflected beam and ΔR is the difference output. Magnitude and phase data were obtained in a mT static magnetic field by scanning and detecting at the frequency of the sinusoidal drive current using an EG&G Model 7265 Lock-in Amplifier.

Results obtained by scanning the frequency of the current through a $500 \times 2 \mu\text{m}$ xylophone bar with $4 \mu\text{m}$ and $10 \mu\text{m}$ wide supports and at a pressure of 35 mT are shown in figure 4 a and b, respectively. The resonance frequencies and Q-factors of the two devices are 78.1 kHz and 6700, and 95.6 kHz and 7500. For reference, the predicted frequency for a polysilicon free-free resonating bar (assuming a Young's modulus of 160 GPa) is 69.2 kHz. The higher measured values were attributed to the torsional resistance offered by the support beams [8].

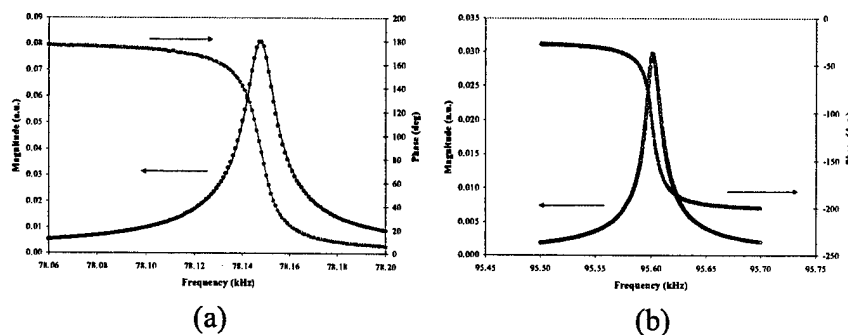
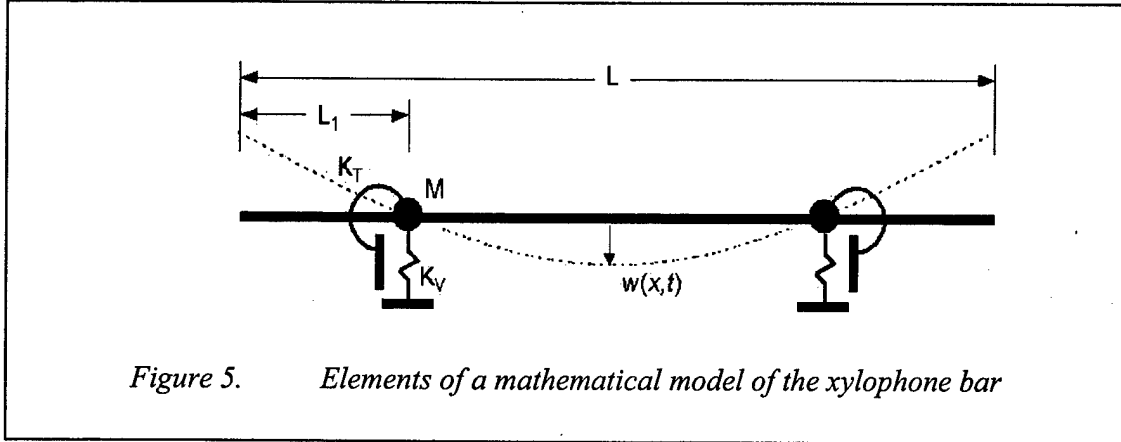


Figure 4. Frequency scans for a $500 \times 2 \mu\text{m}$ xylophone bar with $4 \mu\text{m}$ (a) and $10 \mu\text{m}$ wide (b) supports and at a pressure of 35 mT.

A mathematical model of the xylophone magnetometer incorporating an approximation for the mass and stiffness contributions of the support arm was developed to test the validity of the above notion. Essential elements of the model are shown in figure 5. The two support beams are modeled as vertical and torsional springs (with spring stiffness K_V and K_T , respectively) and a concentrated mass, M .



The dashed line represents the fundamental flexural mode of vibration of the beam. There are two lower frequency modes associated with the flexural vibration of the support arm, but these are not of interest in this study as there is negligible deformation of the resonator bar.

In the current study, the resonator is modeled as a beam based upon the Bernoulli-Euler theory. Use of this theory, rather than the more complex Timoshenko theory, is justified because the wavelength of vibration is much larger than the thickness of the beam. When the vibration wavelength is of the same order as the beam thickness, the effects of shear deformation and rotary inertia included in the Timoshenko theory become important. The partial differential equation governing the motion of a Bernoulli-Euler beam is given by

$$EI \frac{\partial^4 w(x,t)}{\partial x^4} + \rho A \frac{\partial^2 w(x,t)}{\partial t^2} = 0, \quad (6)$$

where $w(x,t)$ is the transverse displacement at any position x along the beam and at any time t , I is the moment of inertia, and A is the cross-sectional area of the beam. The modulus of elasticity, E , and mass density, ρ , for polysilicon are 160 GPa and 2320 kg/m³, respectively. The beam resonator has twenty 5 μm \times 5 μm holes spaced along its centerline to assist in the release of the polysilicon structure. The mass density of the polysilicon was reduced by 2.6% to account for this mass loss, but the effect on the stiffness is considered negligible. Solution of Eq. (6) requires the resonator be divided into three segments: the two cantilevers and the central span between the two support arms. This leads to twelve simultaneous equations governing force and displacement compatibility between the three beam segments and for the two free ends. The

frequencies that cause the determinant of the resulting 12×12 matrix to vanish are the natural frequencies of the system. However, because the two low frequency support arm modes are not of interest, the 12×12 matrix can be reduced to a 5×5 matrix [see Eq. (2)]. This significant reduction in matrix size is accomplished by taking advantage of the fact that the support points are at the nodes of the fundamental flexural mode and their displacement is ideally zero. The first flexural mode shape is also symmetric about the beam mid-span, which allows further simplification. In this reduced form, only the support beam torsional stiffness, K_T , contributes.

The natural frequency of the first flexural mode of the xylophone bar is then determined from the lowest value of α that causes the determinant to vanish:

$$\begin{bmatrix} [\sin(\alpha) + \sinh(\alpha)] & [\cos(\alpha) + \cosh(\alpha)] & 0 & 0 & 0 \\ [\cosh(\alpha) + \cos(\alpha)] & [-\sin(\alpha) + \sinh(\alpha)] & -1 & 0 & -1 \\ [\sin(\alpha) - \sinh(\alpha)]\alpha & [\cos(\alpha) - \cosh(\alpha)]\alpha & -K & -2\alpha & -K \\ 0 & 0 & \cos(r\alpha) & -[\sin(r\alpha) + \sinh(r\alpha)] & \cosh(r\alpha) \\ 0 & 0 & -\cos(r\alpha) & [\sin(r\alpha) - \sinh(r\alpha)] & \cosh(r\alpha) \end{bmatrix} = 0 \quad (7)$$

The parameters K and r in Eq. (7) are given by

$$K = \frac{K_T L_1}{EI}, \quad L_1 = 0.224L, \quad \text{and} \quad r = \frac{L}{2L_1} - 1 \approx 1.232,$$

where the length L_1 is the distance from the ends of the xylophone bar to the center of the supports and the torsional spring stiffness, K_T , is derived assuming the xylophone bar applies a concentrated torque at the mid-span of the support arm. Hence,

$$K_T = \frac{4J_s G}{L_s} \quad (8)$$

where $G = 65$ GPa is the shear modulus for polysilicon, L_s is the length of the support arm, and J_s is a torsional constant that relates the angle of twist to the applied torque and is given as

$$J_s = ab^3 \left[\frac{1}{3} - 0.210 \frac{b}{a} \left(1 - \frac{b^4}{12a^4} \right) \right] \quad (9)$$

The constants a and b are the width and thickness of the support beam, respectively. In this context, the thickness is defined as the lesser of the two cross-sectional dimensions.

The smallest non-zero α satisfying Eq. (7), α_0 , is used to determine the natural frequency, f_{Torsion} , of the first bending mode including the effects of the support arm torsional resistance:

$$f_{Torsion} = \frac{\alpha_0^2}{2\pi L_1^2} \sqrt{\frac{EI}{\rho A}} \quad (10)$$

The form of this expression is very similar to that of the free-free beam, where the first bending mode frequency, f_{Free} is given by

$$f_{Free} = \frac{\beta^2}{2\pi L^2} \sqrt{\frac{EI}{\rho A}}, \text{ with } \beta \approx 4.73 \quad (11).$$

The calculated ratio of the these two frequencies is simply

$$\frac{f_{Torsion}}{f_{Free}} = \left(\frac{\alpha_0 L}{\beta L_1} \right)^2 \approx 0.891 \alpha_0^2 > 1 \quad (12)$$

The measured natural frequencies for each of the three variants of the polysilicon xylophone bar are plotted in figure 6. The theoretical frequencies, as outlined above, are plotted as the continuous curve. The average percent error in the theoretical values is less than 1%. The tendency to underestimate the actual resonance frequencies may be a consequence of: (a) assuming the applied torque to be concentrated at the mid-span rather than distributed over the 50 μm support arm; (b) the assumptions made in deriving the torsional spring stiffness of the support arms; or (c) variations in manufacturing tolerances during processing.

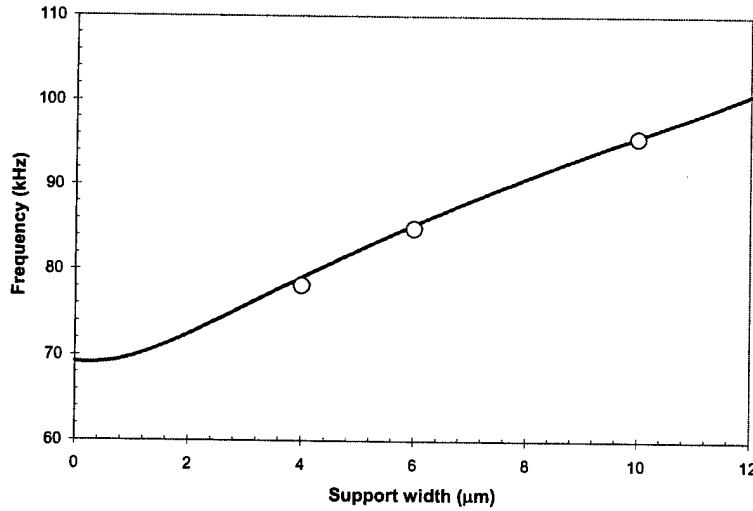


Figure 6. Resonance frequency as a function of support arm width for 500x 50 μm polysilicon xylophone 2 μm thick. The solid line is the theoretical curve. The circles represent measured data.

A plot of the output response of the polysilicon xylophone magnetometer with 4 μm support arm widths as a function of impressed magnetic flux density up to 150 μT is

shown in figure 7. The superimposed line is a least-squares fit to the data, and it is apparent that the magnetometer response is linear over the range of magnetic flux density shown. An estimate of the ultimate noise floor of the xylophone magnetometer, based on thermomechanical noise (Brownian motion due to the Langevin force) and, to a lesser extent, Johnson noise (current noise that couples with the magnetic field), yields a value of the order of $100 \text{ pT} \cdot \text{A}/\sqrt{\text{Hz}}$. This estimate calls out the very important role that the amplitude of the drive current plays in determining the ultimate field sensitivity of xylophone bar magnetometers. The decreased sensitivity of these initial polysilicon devices, when compared to conventional ($5 \times 0.5 \times 0.09 \text{ mm}$) devices chemically milled from CuBe foil, is identified as being a direct result of the high sheet resistivity of the polysilicon material ($10 \text{ } \Omega/\text{square}$) and its lower current carrying capability.

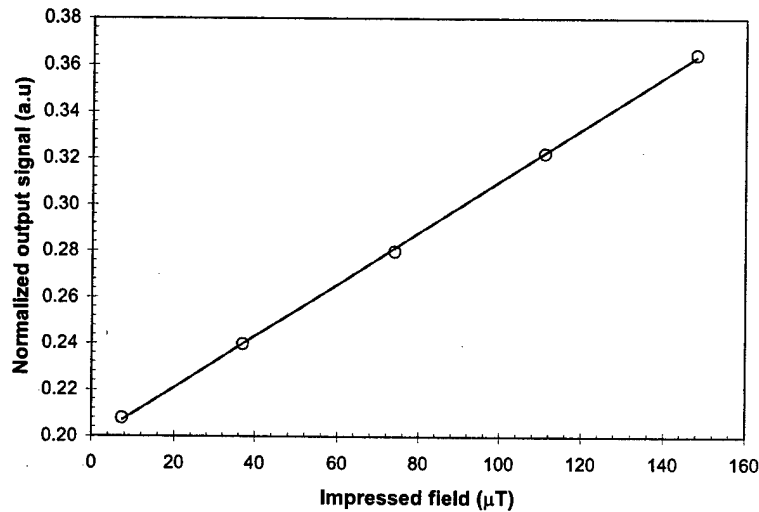


Figure 7. Output response of a $500 \times 50 \times 2 \text{ } \mu\text{m}$ xylophone magnetometer as a function of impressed magnetic flux density

It is well known that air pressure greatly influences the performance of MEMS resonators and an example of this effect on the xylophone with $4 \text{ } \mu\text{m}$ wide arms is shown in figure 8. For this measurement, the magnetic flux density was on the order of $10 \text{ } \mu\text{T}$ (Earth + other background fields) and the xylophone current was $22 \text{ } \mu\text{A}$. The test chamber pressure was varied between 15 mTorr and 85 mTorr and the resulting Q-factors were determined to be $21,950$ and $2,780$, respectively. The 9 Hz decrease in resonance frequency at the lower pressure is believed to be due to thermal effects (lower stiffness). Moderate temperature sensitivity of the resonance frequency has also been observed at constant pressure by varying the intensity of a broad illumination source or by repositioning the mW beam deflection laser. There has also been evidence that mechanical energy losses at resonance contribute enough thermal energy to measurably

lower the resonance frequency of a device.

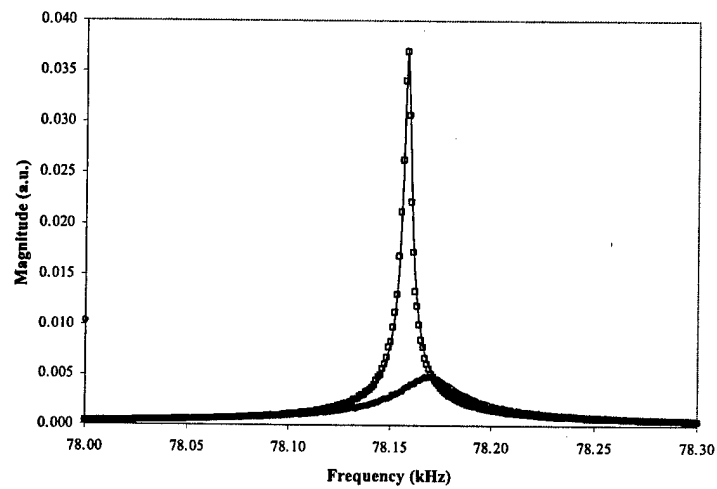
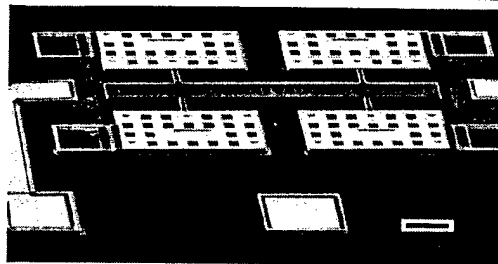


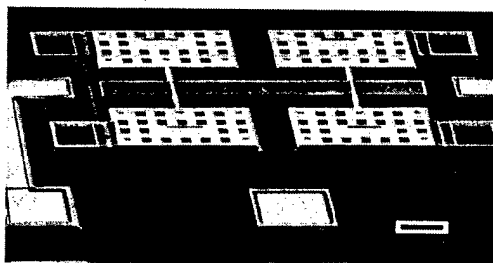
Figure 8. Response of $500 \times 50 \mu\text{m}$ xylophone with $4 \mu\text{m}$ supports at 15 mTorr (squares) and 85 mTorr (circles).



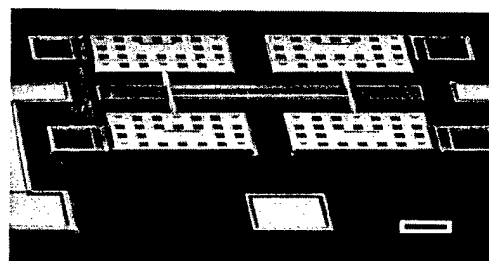
(a)



(b)



(c)



(d)

Figure 9. SEM micrographs of MUMPs30 poly2 devices with gold deposited on the electrodes (a), as partial stripes on the support arms (b), as full stripes on the support arms (c), and, as stripes along the xylophone bar between the support arms (d).

Various designs to decrease the resistance of polysilicon devices were laid out and manufactured on the MUMPs30 production run. In these new designs the drive current to the magnetometer is fed from both sides, giving an immediate doubling of the drive current capability. In addition, magnetometers were manufactured from poly1/poly2 layers and the use of gold stripes deposited on various parts of the xylophone was examined. Also included on the die were various geometries of poly0 and poly2 capacitive plates. SEM micrographs of released and packaged MUMPs30 poly2 devices with gold deposited on the electrodes, as partial stripes on the support arms, as full stripes on the support arms, and, as stripes along the xylophone bar between the support arms, are reproduced in figure 9.

Characterization of these devices showed that the poly1/poly2 500 x 50 x 3.5 μm bars with gold deposited on only the electrodes [figure 9(a)] have resonance frequencies of 165 kHz and Q-factors of between 30,000 and 40,000 at low pressures. The same bars with full gold strips on the support arms [figure 9(c)] have increased resonance frequencies to 168 kHz, due to the increased stiffness of the support arms, and Q-factors of 10,000. The bars with the gold strips along the xylophone bar [figure 9(d)] have decreased resonance frequencies of approximately 164 kHz, due either to mass loading of the bar or to the decreased effective Young's modulus, and Q-factors in excess of 10,000. From these results and from those from similar devices manufactured on subsequent MUMPs runs, it is concluded that although the use of gold increases the current carrying capacity, there is a concomitant decrease in Q-factor. As a result there is little, if any, increase in overall sensitivity.

3. HYBRID MAGNETOMETER

Before undertaking detailed design, a study was made of the Analog Devices' BIMOSIIE(iMEMS) process. This process integrates an analog IC process with MOSFETs, BJTS, diodes and resistors with MEMS to create electro-mechanical sensors. This process is used to fabricate the ADXL family of accelerometers sold by Analog Devices. The accelerometers use interdigitated electrodes to form a capacitive sensor whose movements are restricted to a plane parallel to the die surface. Although the process is well suited for this application, it has been highly optimized and designs that deviate considerably from this method of sensing movement are not easily implemented.

According to the design rules obtained via the MEMS Exchange, the sensor area is defined by the mask layer MOAT. In this region, all structural oxides will be removed to allow for release of the mechanical components of the sensor. As a direct consequence, the only elements that are allowed in the sensor region are structural polysilicon for beams (BEAM), polysilicon anchors (ANCH), spacer oxides (MOBE) and an implanted wiring layer (EMIT). Therefore the only method of constructing the xylophone based magnetometer would be to use BEAM as the vibrating bar over an area of EMIT to form the plate of a sense capacitor.

This technique leads to several problems for this design. The capacitive coupling between the BEAM and plate implemented in the EMIT layer will not be as strong as the

present Cronos based design. The BIMOSIIE design manual specifies that the structural poly is $1.6\mu\text{m}$ above the silicon nitride layer that coats the die. The nitride thickness was not specified. However, the $1.6\mu\text{m}$ gap is already considerably larger than the $0.75\mu\text{m}$ gap available between the poly2 and poly1 layers on the Cronos MUMPs process. Therefore, the capacitance between the sense plate and the beam will decrease. More significantly, the percent change in the capacitance as the bar is deflected will be reduced, assuming similar deflections for both devices.

A second problem arises by implementing sensing capacitor plates in the EMIT layer. The EMIT layer is an N+ implanted region within the p-type silicon substrate. This forms a reverse biased diode between wiring drawn in EMIT and the substrate. Consequently, there is a large junction capacitance between the plates fabricated in the EMIT layer and the silicon die, which is electrically connected to the circuit ground. If the coupling area of the structure is $100 \times 50\mu\text{m}^2$, the stray capacitance to ground is 630fF – at least 20 times larger than the sensor capacitance. This large stray capacitance would significantly impact the first stage amplifier from the sensor.

Finally, it is desirable for the xylophone to present a low impedance to the drive circuitry. The POLY material used to form the bar is $10\Omega/\text{sq}$, which is comparable to the present design. However, the stray resistance in the wires and contacts to/from the bar is quite large. The design rules do not allow POLY or METAL wires to cross the boundary between the circuit and sensor areas. Therefore, we would be forced to use wires made in the EMIT layer to interconnect the polysilicon BEAM and the circuitry. The design manual specifies that the resistance of a single, minimum size contact between the polysilicon BEAM and the EMIT wire is $1.2\text{ k}\Omega$. Additionally, the resistance of the EMIT layer wire is $14\Omega/\text{sq}$. The total DC impedance will then be a few kilo-ohms – at least an order of magnitude larger than the present design. Additional AC loading will also be present because of the junction capacitance of the wiring. Running the circuits at a lower drive current is not an acceptable means of addressing the problem since the lower current results in less sensitivity to applied magnetic field.

The Analog Devices BIMOSIIE process may seem attractive for use in creating MEMS devices with integrated signal conditioning and control electronics on a single die. However, the level of optimization that has been performed to construct the ADXL accelerometers, does not allow for simple migration of alternate sensor designs. It is concluded that the polysilicon xylophone bar magnetometer project would benefit more by taking a hybrid approach to the system design. The hybrid would consist of two dice, one containing the mechanical structures and a second die containing the associated drive and sense electronics. This initial design of the capacitive sense using a charge sampling circuit was fabricated using the AMIS $0.8\mu\text{m}$ process through MOSIS.

The purpose of the charge sampling circuit is to measure the deflection of the magnetometer transducer shown in figure 10. A current, I_{ac} , is fed from end1 to end2. In the presence of a magnetic field the Lorentz Force causes the beam to deflect. When the beam bends down in the center, the middle plate capacitor increases and the side plate capacitors decrease. Likewise, when the beam bends up the middle plate capacitor

decreases and the side plate capacitors decrease. The peak capacitance change to a $1\mu\text{T}$ field is approximately 0.1 %.

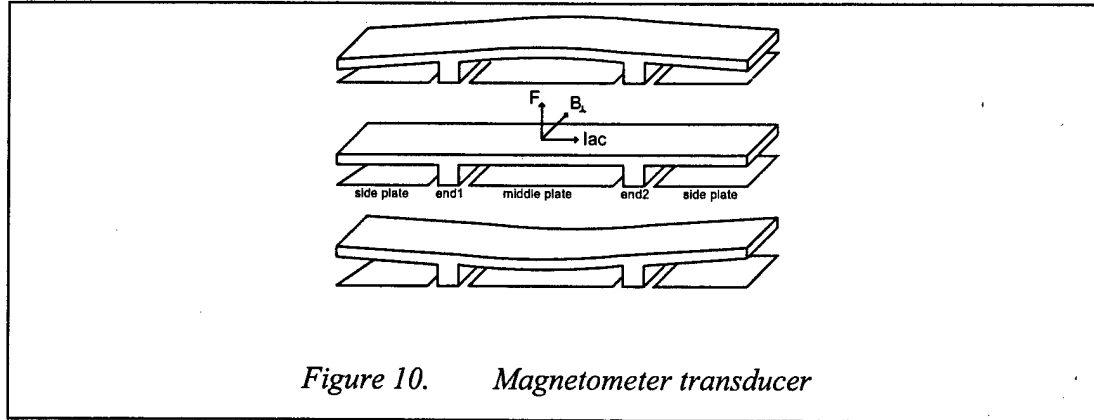
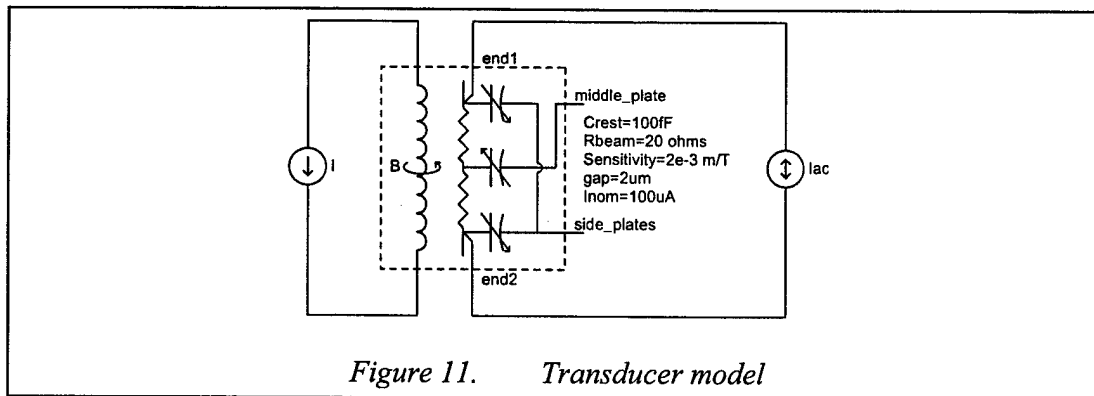


Figure 11 shows a circuit model for the transducer. Note that the top plate of each capacitor is also the beam. Resistance has been added to model the resistance of the beam material as shown. Because the top plates are connected to the beam, they cannot be used as the summing node in a switched capacitor circuit. Thus, two circuits were investigated that uses the bottom plates in the summing node. The first is a circuit that uses charge redistribution to determine the difference in the middle and side capacitors. The other more robust design uses active common mode subtraction in determining the capacitance difference. Both circuits are described and an explanation given why the active common mode subtraction was chosen.



The charge redistribution switched capacitor network is shown in figure 12. The clocks are shown in figure 13. Clocks ϕ_1 and ϕ_2 are non-overlapping clocks. Clocks ending with a 'd' are slightly delayed versions. For example, ϕ_{2d} is slightly delayed from ϕ_2 . In the case of a delayed clock, care is taken to ensure the delayed clock does not overlap the next clock phase. For example, ϕ_{2d} does not overlap ϕ_1 . In this circuit ϕ_1 is split in to two phases ϕ_{1-X} and ϕ_{1-Y} .

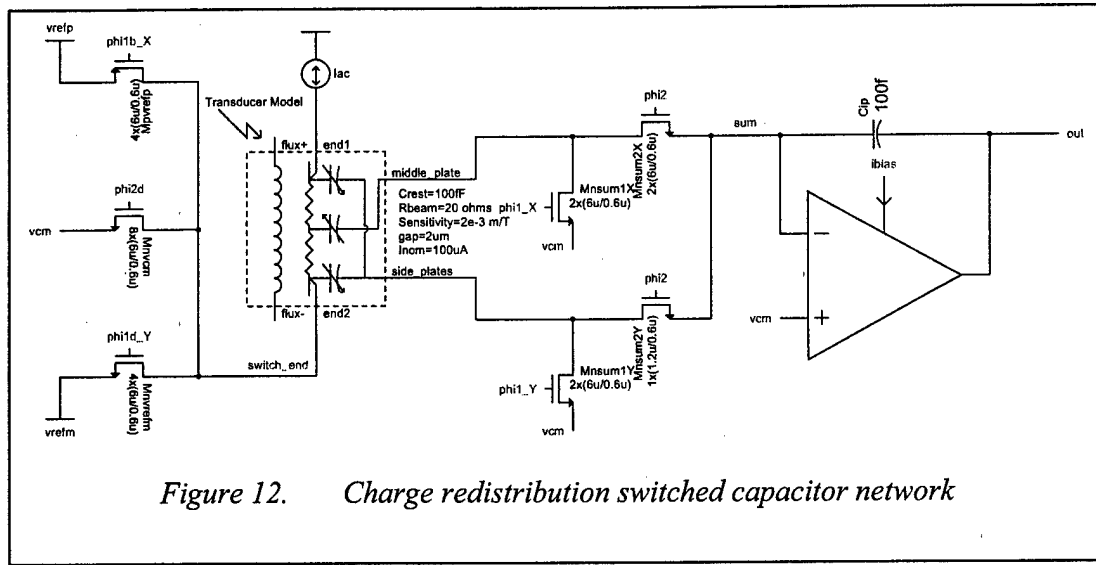


Figure 12. Charge redistribution switched capacitor network

Assume that the supply rails v_{dda} and v_{ssa} are at the 5V and 0V respectively. Also, the common mode voltage, v_{cm} , is 2.5V. The positive reference voltage, v_{refp} , is 4V. The negative reference voltage, v_{refm} , is 1 V. The current source I_{ac} can sink and source current from v_{refp} , v_{cm} , and v_{refm} .

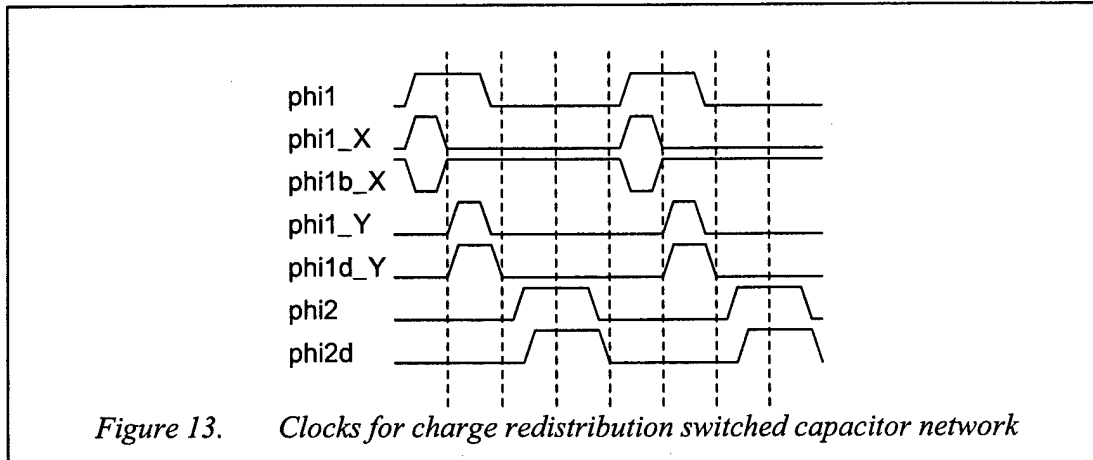


Figure 13. Clocks for charge redistribution switched capacitor network

During ϕ_{1-X} the middle plate capacitor is charged to a positive reference voltage " $v_{refp} - v_{cm}$ ". During ϕ_{1-Y} the side plate capacitors are charged to a negative reference voltage " $v_{refm} - v_{cm}$ ". For simplicity, ignore the voltage across the beam, " $I_{ac} * R_{beam}$ ". More on the effect of this voltage drop will be explained in detail below.

During ϕ_2 the top plates are connected to v_{cm} and both the bottom plates are connected to the summing node of the inverting amplifier. The charge on the middle and side capacitors redistribute and cancel each other out. If the middle plate has more charge, then the virtual ground at the summing node forces this charge to flow across the integrating capacitor, C_{ip} , and increase the voltage of node out. Likewise if the middle

plate has less charge than the side capacitors, then charge is removed from C_{ip} and voltage of node out decreases. The charge on C_{ip} is never cleared. Thus, this circuit is a discrete integrator with equation:

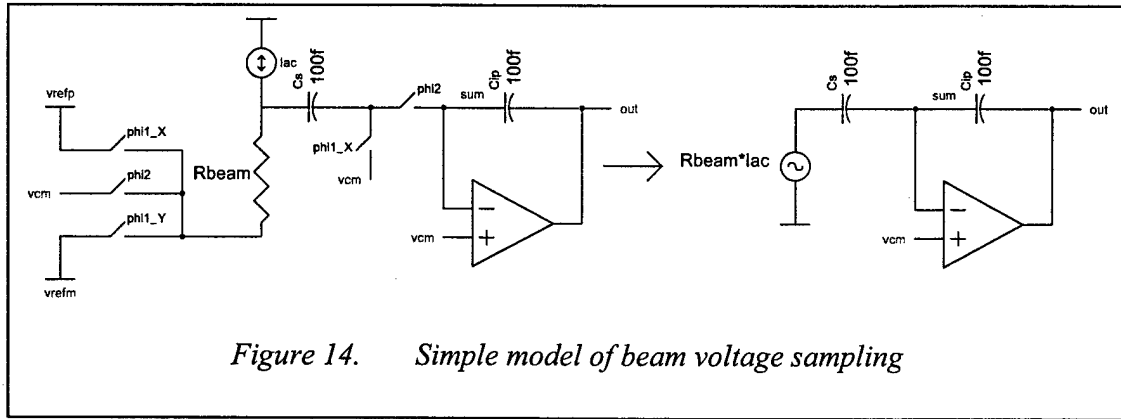
$$out(n) = out(n-1) + \frac{C_x(n-1) - C_y(n-1)}{C_{ip}} \frac{V_{ref}}{2},$$

where

$$\frac{V_{ref}}{2} = v_{refp} - v_{cm} = -(v_{cm} - v_{refm})$$

or

$$out(n) = out(n-1) + \frac{\Delta C(n-1)}{C_{ip}} \frac{V_{ref}}{2}$$



Previously the voltage drop across the beam " $I_{ac} * R_{beam}$ " was ignored. Analysis of the circuit reveals that this voltage will be sampled. Fortunately, the voltage will not be integrated. Because the voltage across the beam is present with the same polarity during both ϕ_1 and ϕ_2 , the circuit can be modeled as a continuous time amplifier as shown in figure 14. The equation for this voltage is:

$$out(n) = \frac{C_s}{C_{ip}} R_{beam} \times I_{ac}(n)$$

Thus, the beam voltage will enter into the measurement. However, it is not integrated like the signal $\Delta C(n)$. This along with the fact that R_{beam} is approximately 20 ohms should help the beam voltage from being a problem in the sensing circuit.

The first problem with the proposed switched capacitor circuit above is converting it to a fully differential circuit. In order to convert it the transducer must be modified to have twice as many capacitors. A fully differential design is required in order to minimize the effects of charge injection and common mode interference.

Another problem with this design is that each transducer capacitor is floating during half of ϕ_{11} . Ideally when the capacitor is not connected it will store its previous voltage. However, due to stray capacitances this will not be the case.

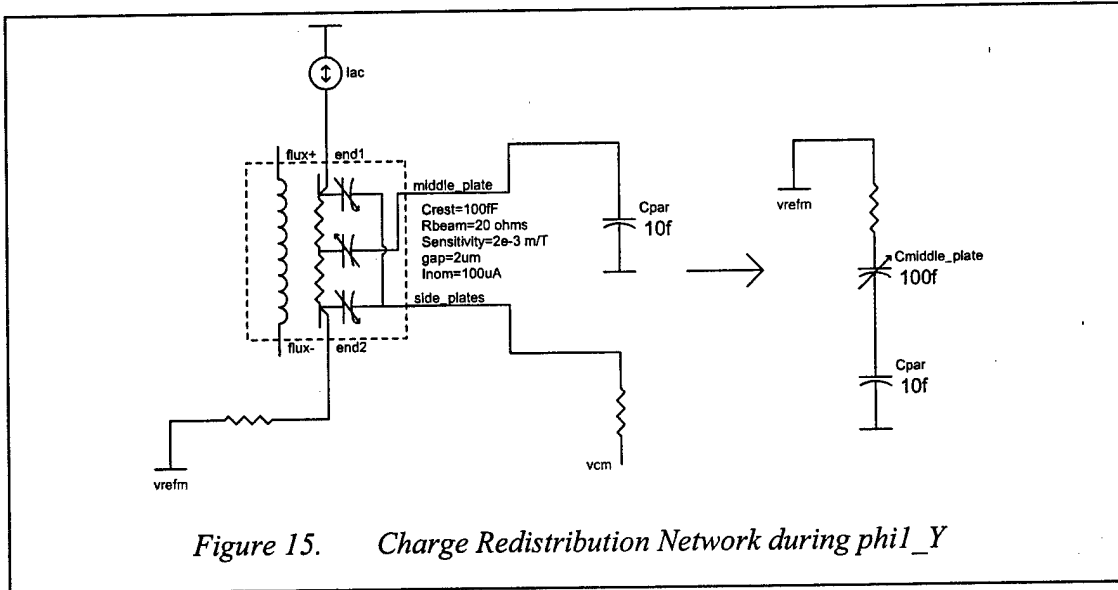
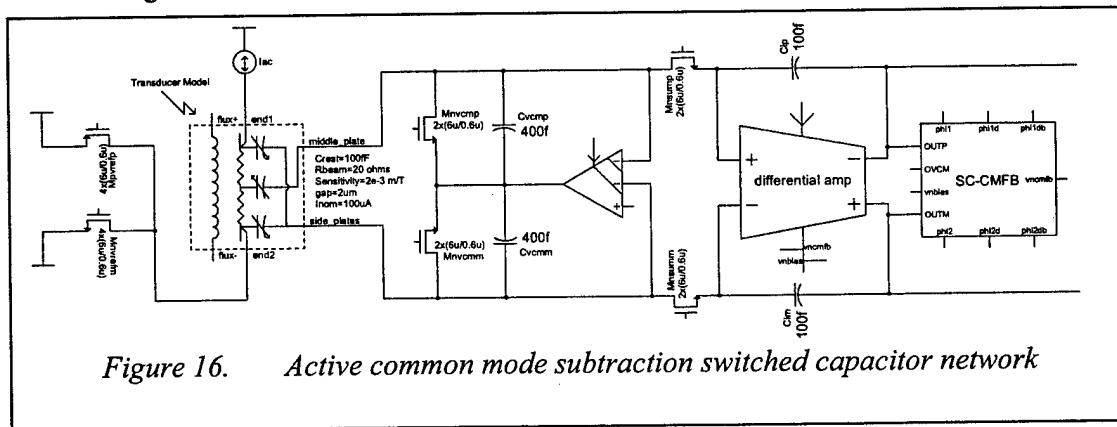


Figure 15 shows the network during ϕ_{1_Y} . During this phase the side plates are charged to the negative reference voltage. A parasitic capacitance of 10fF is shown to illustrate the problem with the floating middle plate capacitor. The parasitic capacitor will cause the middle plate capacitor to sample the v_{refm} voltage. While it may only sample $1/10^{\text{th}}$ of the voltage, this is significant since the capacitance change being measured is only $1/1000^{\text{th}}$ of the resting capacitance.

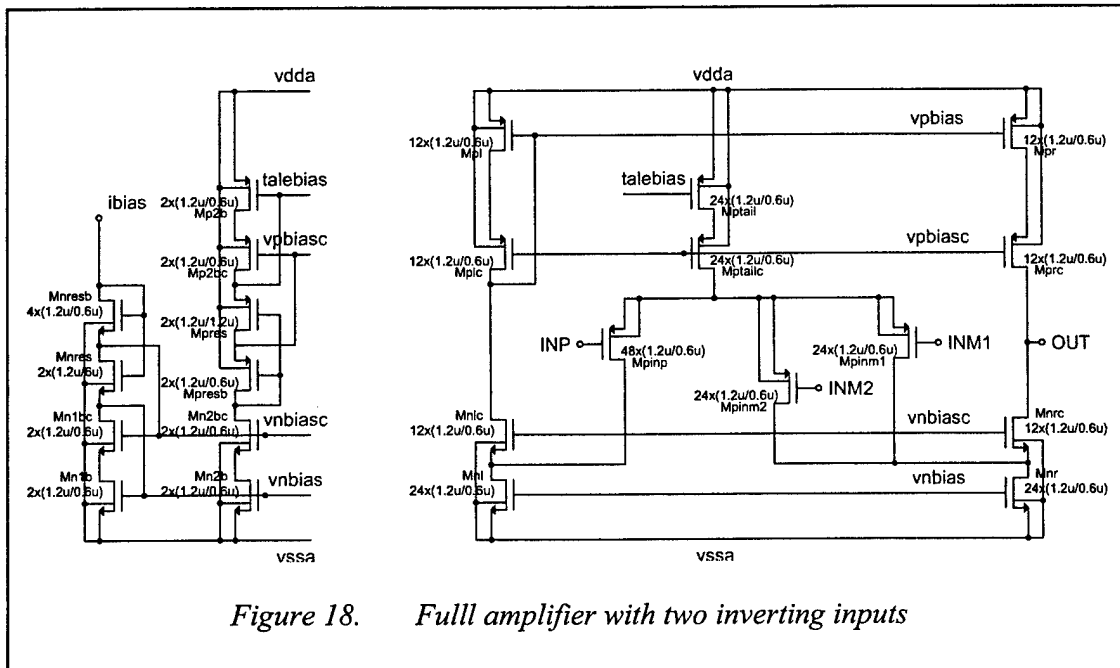
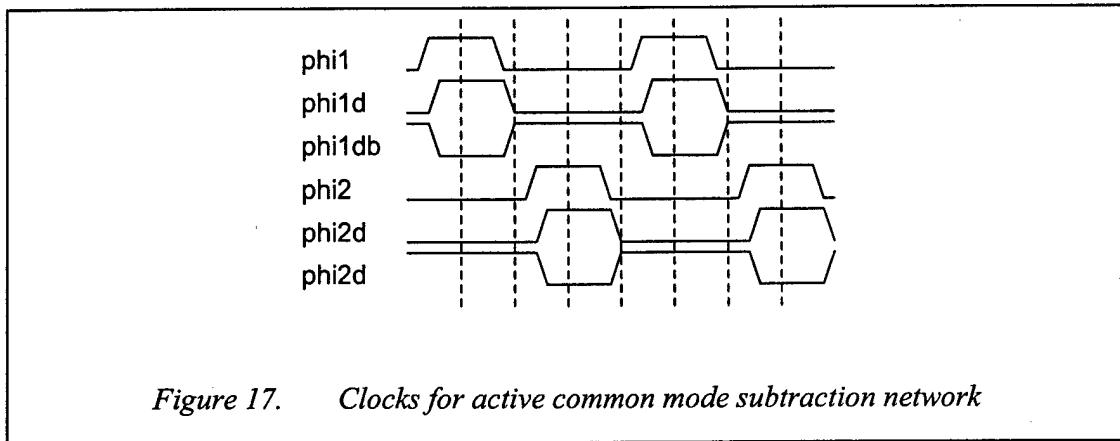
A more robust capacitive sensing network is shown in figure 16. The clock scheme is shown in figure 17. Unlike the circuit in figure 12, this circuit is fully differential without adding more capacitors to the transducer. This circuit uses an amplifier to remove the common mode charge rather than charge redistribution. This is done by the use of the amplifier with two inverting inputs. Details of this amplifier are shown in figure 18.

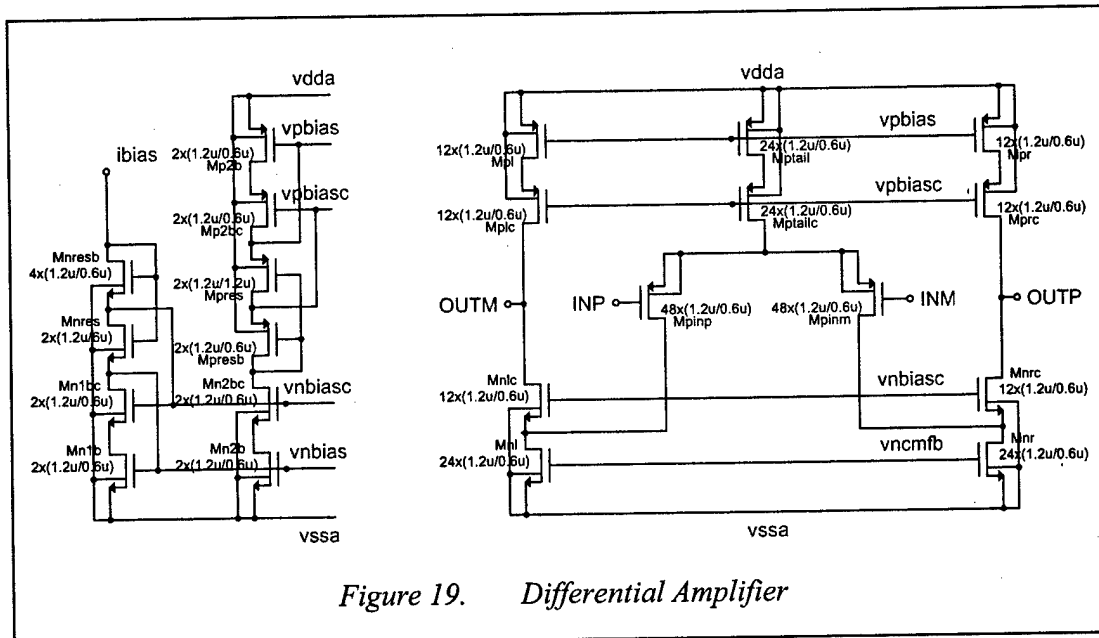


During ϕ_{i1} the amplifier is configured as a unity gain buffer and the middle and side plates of the transducer are held at v_{cm} . During ϕ_{i2} the amplifier continues to hold the plates at v_{cm} by subtracting of the common mode charge on the transducer capacitors through the capacitors C_{vcmp} and C_{vcmm} . The fully differential amplifier (figure 19) moves the difference charge to the integrating capacitors C_{ip} and C_{im} . Thus, the discrete time equation of the output voltage is:

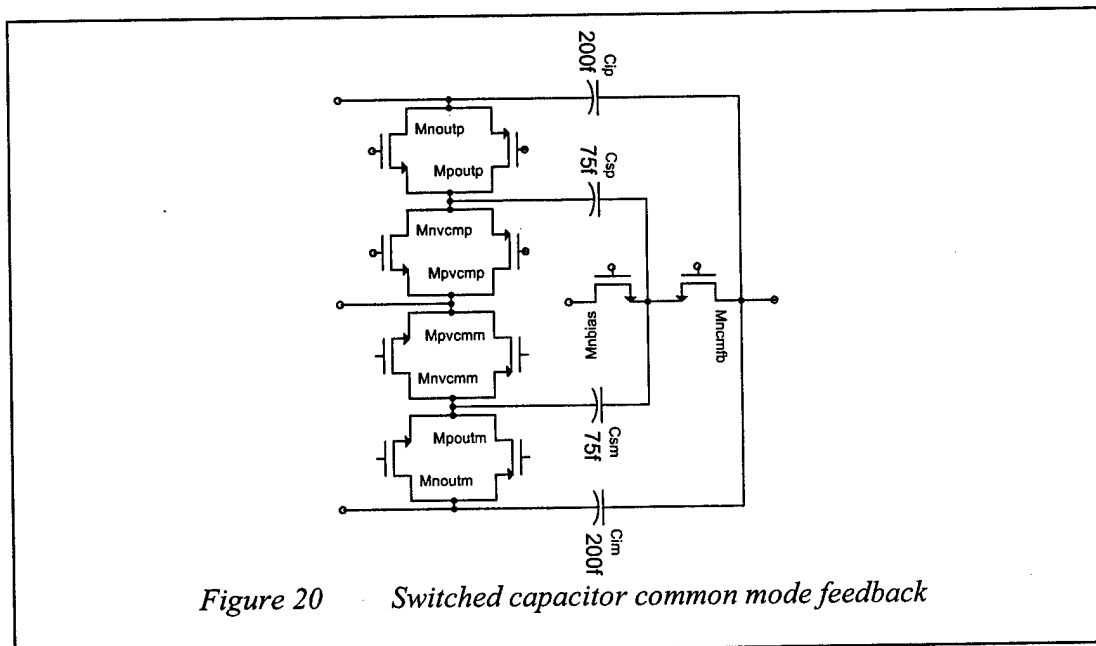
$$out(n) = outp(n) - outm(n) = out(n-1) + V_{ref} \frac{\Delta C(n-1)}{C_i}, \quad C_i = C_{ip} = C_{im}$$

The differential amplifier's output common mode voltage is held at v_{cm} by the switched capacitor common mode feedback circuit in figure 20. Both amplifiers have a nominal bias current, i_{bias} , of $5\mu A$.



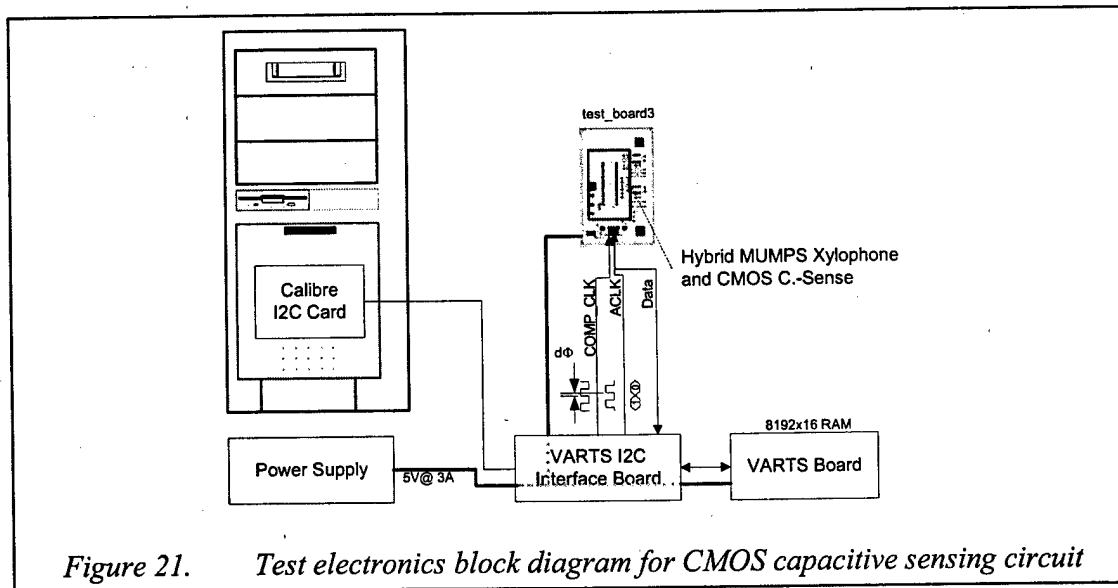


The active common mode subtraction network has several advantages over the charge redistribution network. First, it is fully differential. Thus, it will have better rejection of charge injection and interference. Second, it has a simpler clocking scheme and does not have the floating capacitance problem.

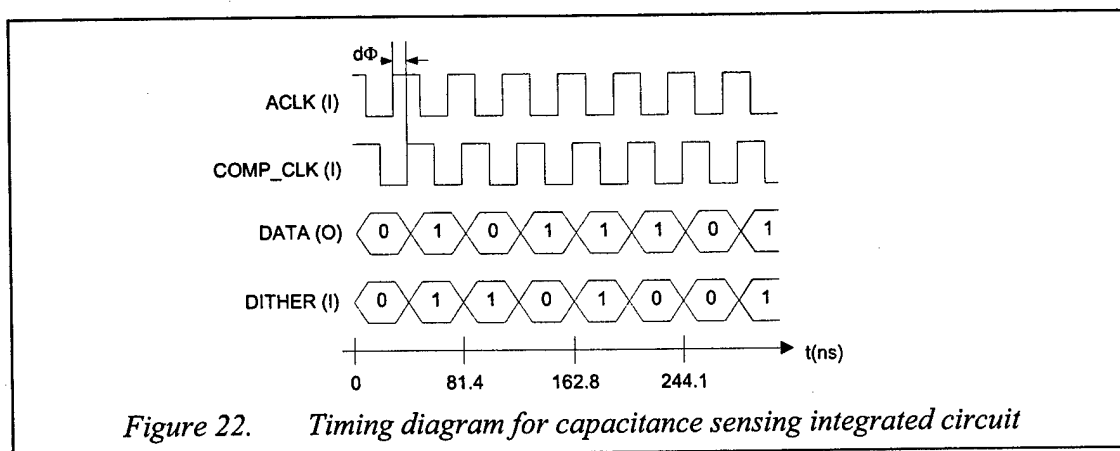


This circuit was verified with SPICE simulations and was fabricated using the AMIS 0.8 μm process through MOSIS.

The test setup used to evaluate the CMOS capacitance sensing circuit is shown in figure 21. The capacitive sensing integrated circuit is mounted on test_board3. The VARTS I2C interface board and VARTS board contain programmable logic and interface logic to allow data collection and communication between the PC and test_board3. An external power supply is used to provide supply voltages for test_board3 and other electronics external to the PC.



Two digital clock signals, ACLK and COMP_CLK, are used to control the capacitive sensing circuit timing. A pseudo-random digital signal (DITHER) is applied to the circuit to help reduce in-band tones. The value of the dither signal changes for each cycle of the COMP_CLK clock signal. The sensed capacitance undergoes a 1-bit analog-to-digital conversion and the digital output is updated once during each cycle of the ACLK clock input signal. A timing diagram of the capacitive sensing circuit digital interface is shown in figure 22.



Since the interface between to the CMOS electronics is programmable, two test cases were implemented.

In case (1), the phase difference ($d\Phi$) between the comparison clock test signal (COMP_CLK), as it leaves the VARTS Board, and the switched-capacitor (S-C) circuit clock test signal (ACLK) is approximately 90° . In case (2), $d\Phi$ is approximately 180° .

The data is retrieved and stored in a PC using a Matlab program which controls the I2C card. Once retrieved, the frequency content of the data can be plotted and additional post-processing and filtering implemented. Post-processing filters are used to remove the high-frequency quantization noise above the frequency of interest.

In case (1), the signal-to-noise ratio (SNR) was observed to be approximately 6-7dB. In case (2), the signal-to-noise ratio (SNR) was observed to be approximately 8-9dB. Test conditions for each case are shown in Table 1.

Test Case	Source Freq. (kHz)	Lock-In Freq. (kHz)	Lock-In Signal Magnitude (mV)
Case (1) – a	42.46189	42.46	2.8
Case (1) – b	42.45671	42.45-42.46	2.8
Case (1) – c (No laser)	-	-	-
Case (2) – a	42.45546	42.45	2.9
Case (2) – b (No laser)	-	-	-

Table 1. Test conditions

The frequency of the xylophone beam deflection was controlled by thermally exciting the beam with a laser source modulated by a Stanford Research Systems Model DS345 function generator. The beam deflection was measured using a position sensitive detector (PSD) and an EG&G 7265 DSP lock-in amplifier. There are slight variations in resonant frequency for case (1) and case (2). The reason for this is not fully understood, although it is possible that the DC-field created between the xylophone beam and the capacitive sensing plates is different in each case.

The frequency content of the unfiltered output signal is shown in figure 23 and figure 24 for both cases. Figure 25 and figure 26 show similar data for post-filtered output signals.

The cause of slight variations in resonant frequency for case (1) and case (2) is not fully understood from an electrical standpoint, although it is possible that the DC electric field created between the xylophone beam and the capacitive sensing plates is slightly different in each case, resulting in a change in electrostatic attractive forces (and hence resonant frequency). Alternatively, this variation could be due to slight variations in temperature in each test run.

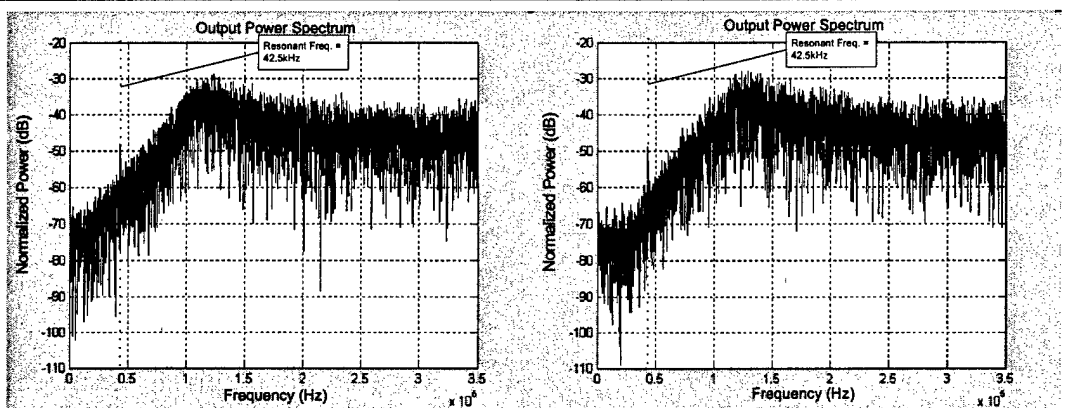


Figure 23. Unfiltered output power spectrum of hybrid MUMPS xylophone magnetometer and CMOS capacitive sense circuit. Comparison of spectra when test signal COMP_CLK phase leads test signal ACLK by 90° (Left) and when COMP_CLK and ACLK are 180° out-of-phase (Right).

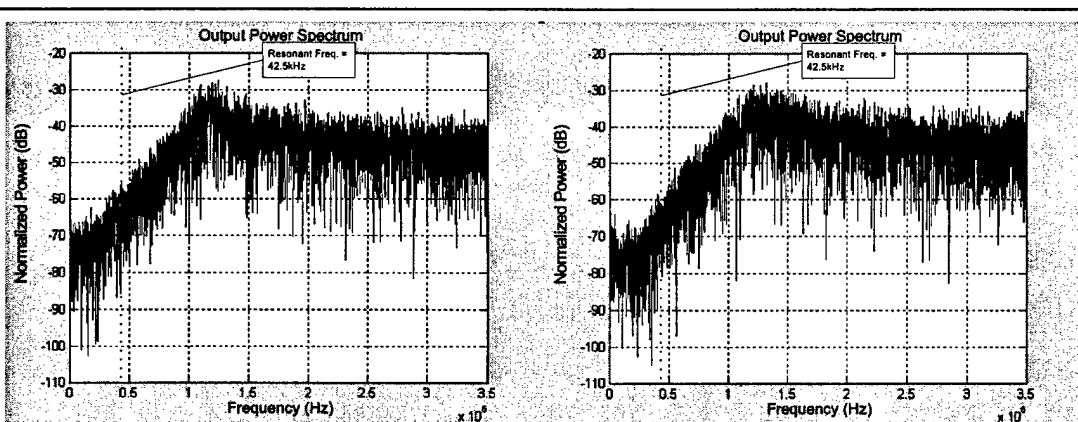


Figure 24. Unfiltered output power spectrum of hybrid MUMPS xylophone magnetometer and CMOS capacitive sense circuit in the absence of xylophone deflection. Comparison of spectra when test signal COMP_CLK phase leads test signal ACLK by 90° (Left) and when COMP_CLK and ACLK are 180° out-of-phase (Right).

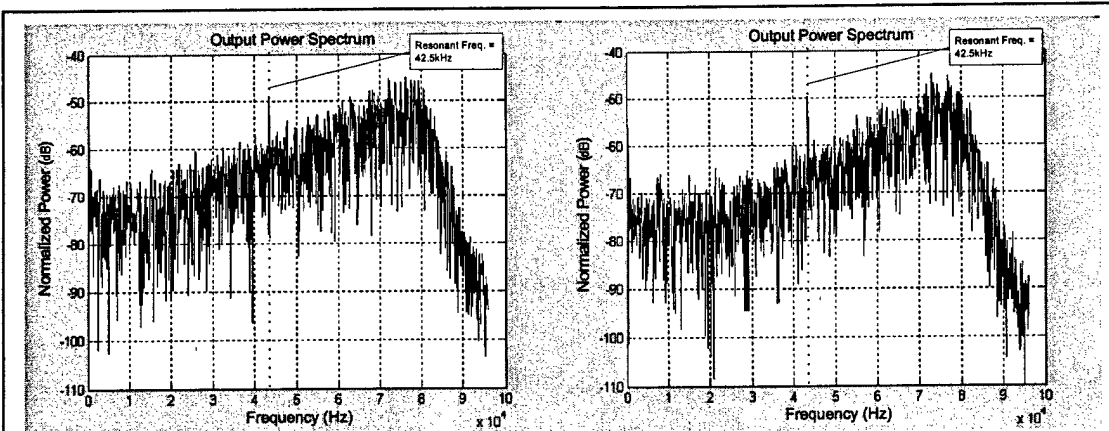


Figure 25. Output power spectrum of hybrid MUMPS xylophone magnetometer and CMOS capacitive sense circuit with multi-stage digital decimation post-filter. Comparison of spectra when test signal COMP_CLK phase leads test signal ACLK by 90° (Left) and when COMP_CLK and ACLK are 180° out-of-phase (Right).

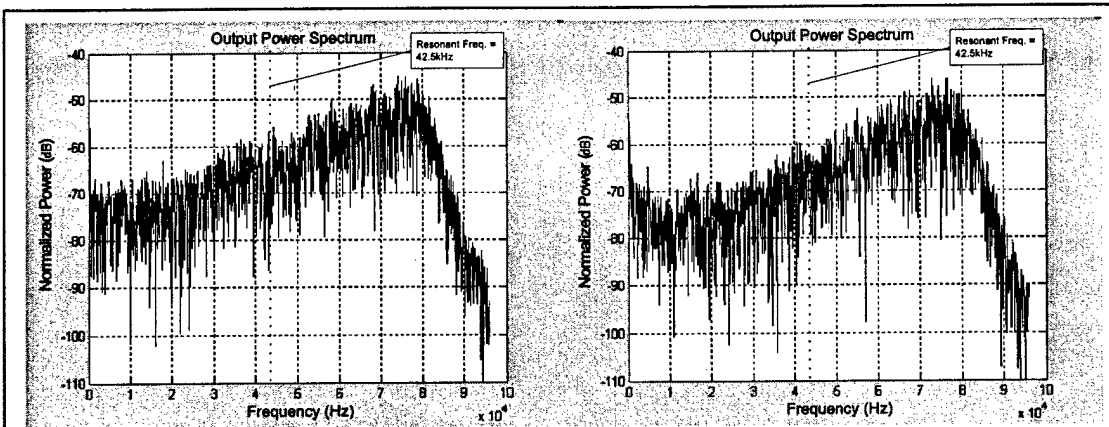


Figure 26. Output power spectrum of hybrid MUMPS xylophone magnetometer and CMOS capacitive sense circuit with multi-stage digital decimation post-filter in the absence of xylophone deflection. Comparison of spectra when test signal COMP_CLK phase leads test signal ACLK by 90° (Left) and when COMP_CLK and ACLK are 180° out-of-phase (Right).

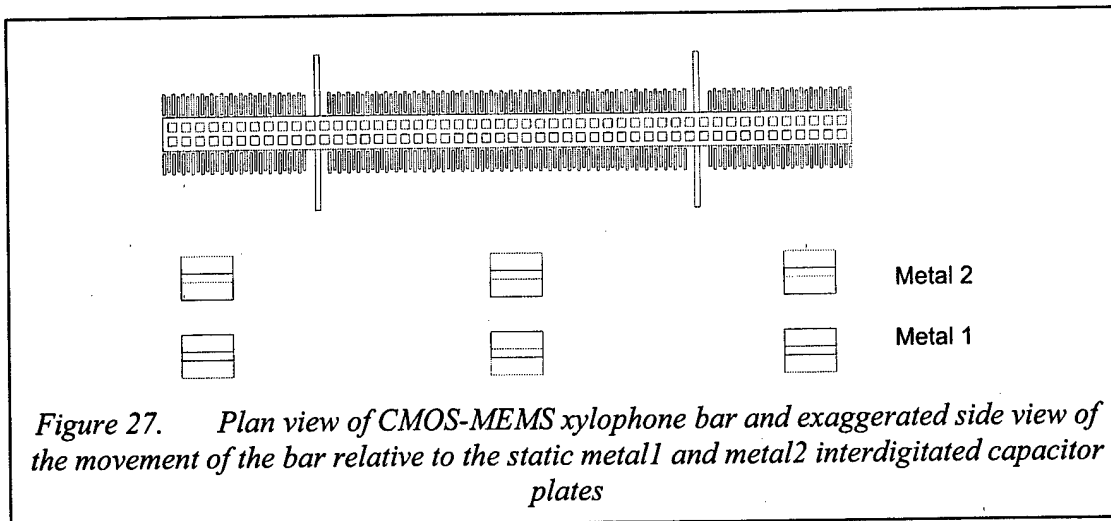
4. CMOS MAGNETOMETER

As noted in section 2 above, the sensitivity of polysilicon xylophone bar magnetometers is limited by the current carrying capacity. Recent advances in fabricating integrated MEMS structures using post-processing of conventional MOSIS-type CMOS foundry structures [9] offer an attractive solution to increasing the current carrying capacity of MEMS-based magnetometers. CMOS MEMS has been around a long time for the fabrication of simple structures.[10] The advent of deep reactive ion etching (DRIE) has allowed the development of complicated and high-definition structures with performances comparable with their polysilicon or silicon-on-insulator equivalents. These structures are composed of combinations of the polysilicon gate layer, the interconnect metallizations, and isolation dielectrics used in standard CMOS processing. Typically, the top metallization layer is used to protect the electronic circuitry from the post-processing etching used to release the micromechanical structures. The metal layers are electrically connected together in conventional comb finger capacitive drive and sense structures so that the comb fingers function in the same way as their homogeneous polysilicon or silicon counterparts. However, metal layers in multi-conductor comb fingers can also be selectively interconnected to form two sidewall capacitors between comb fingers whose capacitances change with displacements perpendicular to the substrate surface. Thus, using CMOS MEMS enables the development of complex micromechanical structures, such as the combination of vibrating bar xylophone magnetometer and x-, y-, and z-axis accelerometers and angular rate sensors, with state-of-the-art capacitive sense performance on a single chip. Custom designs can be obtained either through the DARPA-sponsored Application-Specific MEMS Process Service (ASIMPS) maintained by Carnegie Mellon University or through standard MOSIS-supported CMOS foundries.

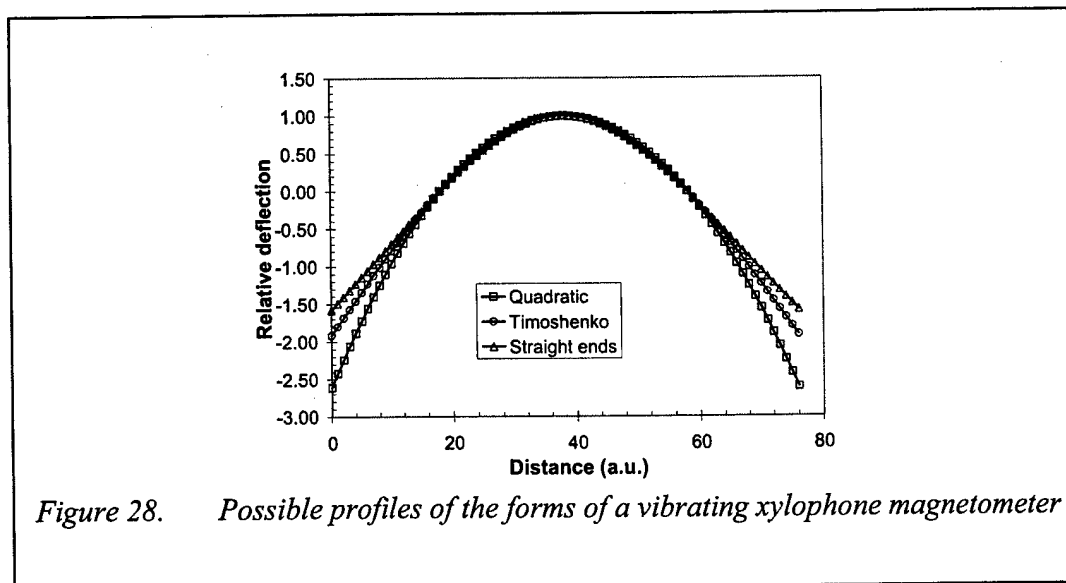
A study was undertaken on the expected performance benefits of MEMS based magnetometers fabricated in CMOS technology. Since a similar layer scheme is available in silicon-on-sapphire (SOS) technology, the potential benefits of alternative optical sensing was included in the study. This was considered relevant since capacitive sensing has limits and there is a need to develop alternative transduction schemes that are compatible with both CMOS and MEMS. The use of a sapphire substrate would allow the development of more sensitive optical transduction schemes.

The model magnetometer structure is depicted in plan view in figure 27, together with an exaggerated view of the movement of the bar relative to the metal 1 and metal 2 interdigitated capacitor fingers, assuming that there is no residual stress in the structure and that in the absence of movement the static and dynamic fingers are parallel.

The main bar is $400 \times 19 \mu\text{m}$ in dimension and the supports are $30 \times 3 \mu\text{m}$. The interdigitated capacitors are $12 \mu\text{m}$ long with width and gap spacings of $1.4 \mu\text{m}$. The overlap between the static and dynamic is assumed to be $10.5 \mu\text{m}$. There are 15 sets of interdigitated fingers on the bar between the ends and the supports and 37 sets between the supports.



One of the unknowns is the form of the xylophone bar while vibrating. Three possible examples are shown in figure 28. These are quadratic, the classical Timoshenko form of a simply supported beam with a concentrated force applied to the center of the bar, and the Timoshenko form in the center of the bar but with straight sections tangential to the bar from the supports to the ends. This latter form is possible from the few laser vibrometer results we have seen from ARL, Adelphi's PZT samples. The Timoshenko form with a concentrated force applied to the center is preferred to that of a uniformly distributed load because the boundary conditions used do not apply to the xylophone magnetometer with finite semi-rigid supports not at the ends. It can be seen that the relative deflection between the supports is quite insensitive to form but there are significant differences at the ends, affecting calculations on capacitive changes with deflection.



The static deflection (d_s) of the xylophone bar with a current I (Amperes, A) passing through it in a magnetic field of B (Tesla, T) is given by[5]:

$$d_s = \frac{5BIL_0^4}{384EI_m} \quad (13)$$

where:

L_0 = length of bar between supports
 E = Young's modulus
 I_m = area moment of inertia
 $= ab^3/12$ for rectangular bar of width a and thickness b

At resonance, and in the absence of non-linear effects, the deflection (d_r) is given by

$$d_r = Qd_s \quad (14)$$

where:

Q = mechanical quality factor.

The thickness of the individual layers (in μm) in typical CMOS and SOS processes, total thickness, and equivalent Young's moduli (N.m^2) and density (kg.m^{-3})

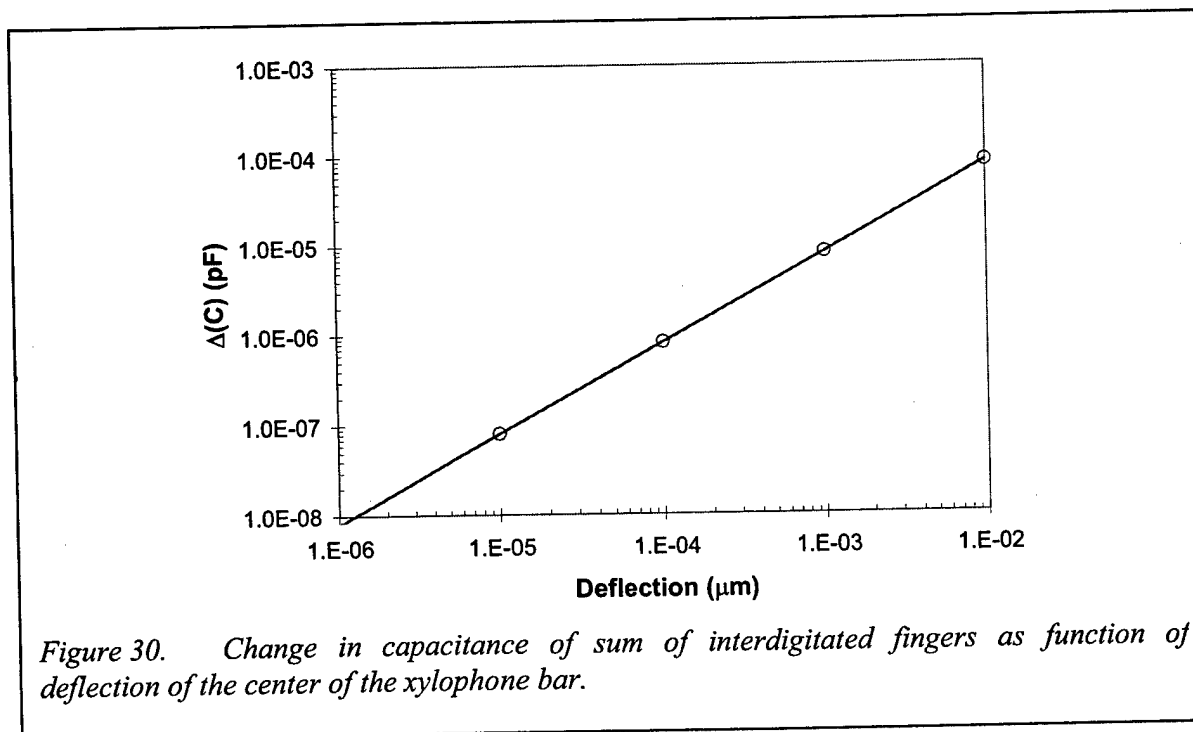
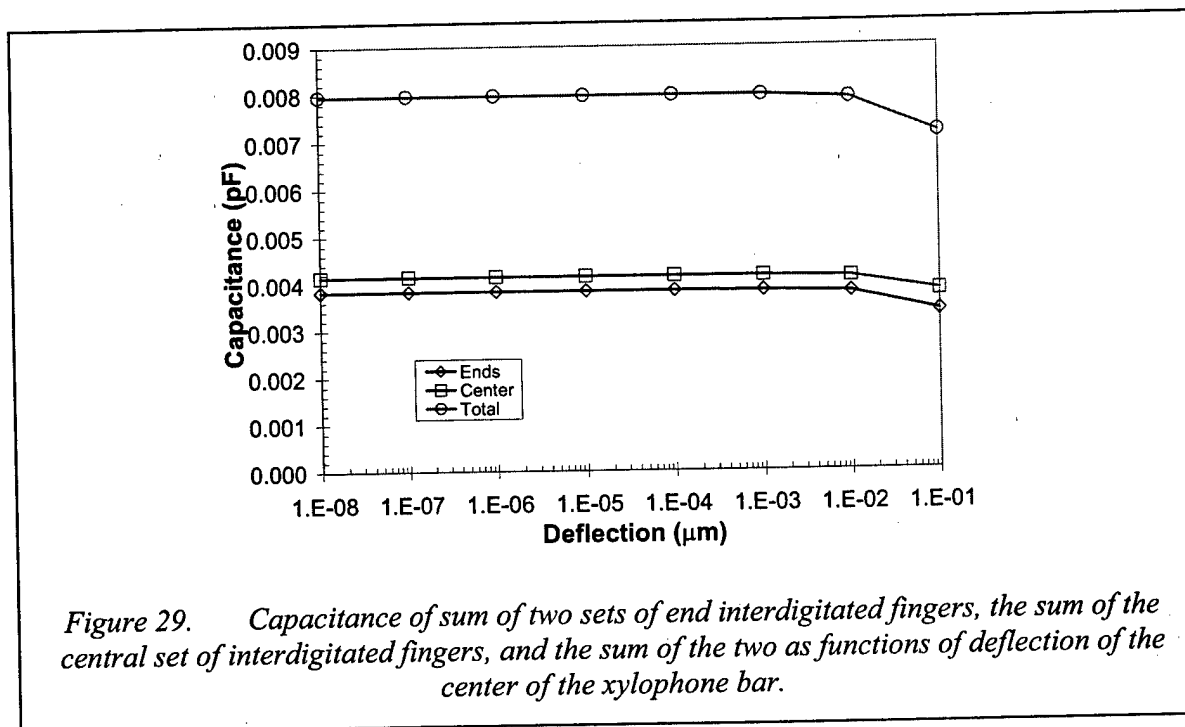
	CMOS	SOS
oxide1 (μm)	0.9	0.5
metal1 (μm)	0.8	1.0
oxide2 (μm)	0.5	0.5
metal2 (μm)	0.8	1.0
oxide3 (μm)	0.4	0.5
metal3 (μm)	1.0	3.0
Total Thickness (μm)	4.4	6.5
Young's modulus (N.m^2)	4.34E+10	5.44E+10
Density (kg.m^{-3})	2.58E+03	2.63E+03

Table 2. Thickness of individual oxide and metal layers, total thickness, and effective Young's moduli and densities for CMOS and SOS processing

are given in table 2.

The capacitance as a function of deflection for the structure shown in figure 27 and the classical Timoshenko form shown in figure 28 is shown in figure 29 for a metal 1 thickness of $0.8 \mu\text{m}$. This figure gives the capacitance of the sum of the two sets of end interdigitated fingers, the sum of the central set of interdigitated fingers, and the sum of the two. The zero deflection values are 3.8, 4.1, and 7.9 fF, respectively. The values for a metal1 thickness of $1.0 \mu\text{m}$ are 4.8, 5.2, and 10.0 fF, respectively. The difference in

capacitance of the total capacitance as a function of deflection for the thickness of both metal's is shown in figure 30.



The maximum current a conductor can carry is limited by Joule heating. For simplicity the supports are modeled as freely suspended filaments in vacuum. In this case the voltage-temperature theorem [11] states that:

$$V^2 = 8 \int_{T_s}^T \kappa_e(T) \rho_0(T) dT = 8 \overline{\kappa_e \rho_0} (T - T_s) \quad (15)$$

where:

V	=	applied voltage
κ_e	=	equivalent thermal conductivity
ρ_0	=	resistivity
T_s	=	temperature of support
T	=	temperature of center of filament

Thus ($V = IR$ and $R = \rho_0 L/ab$):

$$I = \frac{L}{ab} \sqrt{\frac{8 \overline{\kappa_e} (T - T_s)}{\rho_0}} \quad (16)$$

or,

$$(T - T_s) = \frac{\rho_0}{8 \overline{\kappa_e}} \left(\frac{ab}{L} \right)^2 I^2 \quad (17)$$

The absolute maximum temperature corresponds to the melting point (T_m) of the material. From past experience characterizing the polysilicon devices, with support arms typically $45 \mu\text{m} \times 6 \mu\text{m} \times 1.5 \mu\text{m}$, it has been observed that the resonance curves degrade at drive currents of between 1 and 5 mA. The "fusing" current of such support arms is 43 mA for a $T_m = 1410 \text{ K}$. This is to be compared with the observed catastrophic breakdown current of approximately 25 mA. The "effective" temperature differential corresponding to a 5 mA drive current from equation (5) is 15 K. For the purpose of the present study it is assumed that the maximum operating drive current of CMOS and SOS devices will be set by a similar "effective" temperature differential. It is further assumed that oxide3 is a perfect thermal insulator such that the temperature of metal3 (through which the drive current is passed) is independent of the underlying layers. With these assumption the maximum operating current for the CMOS device is 85 mA and for the SOS device is 250 mA.

With these values in place the deflection of a CMOS and SOS xylophone magnetometer with a mechanical Q's of 10,000 as a function of magnetic field is shown in figure 31. From this figure it can be seen that the sensitivities are $4.6 \times 10^{-3} \text{ m.T}^{-1}$ for the CMOS device and $3.4 \times 10^{-3} \text{ m.T}^{-1}$ for the SOS device. For comparison, figure 31 also gives the deflection of a $1000 \times 100 \times 2 \mu\text{m}$ polysilicon device with $Q = 10,000$ and a drive current of $100 \mu\text{A}$.

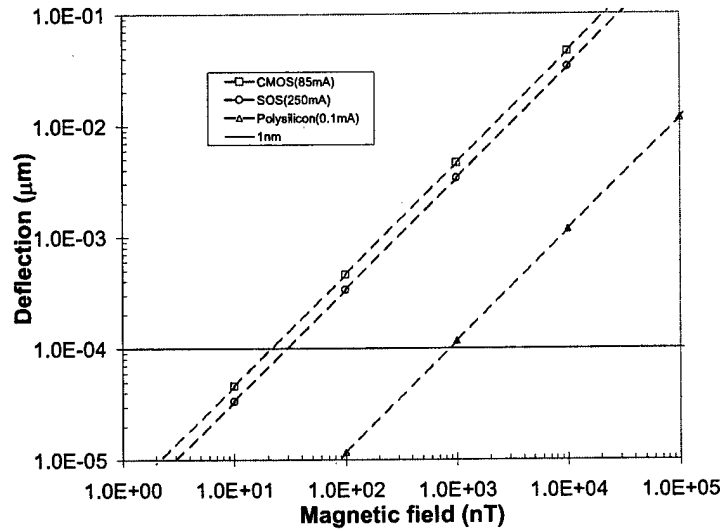


Figure 31. Deflection as function of magnetic field for a CMOS xylophone with $Q=10,000$ and a drive current of 85 mA and a SOS xylophone with $Q=10,000$ and a drive current of 250 mA. Also shown is a $1000 \times 100 \times 2 \mu\text{m}$ polysilicon device with $q=10,000$ and a drive current of 0.1mA.

The signal to noise ratio in the capacitive sampling circuit due to capacitor noise charge is given by [12]:

$$SNR = \frac{OSR}{16kT} \left(\frac{-S}{d_0} \right)^2 B_{\perp}^2 V_{ref}^2 C_0 \quad (18)$$

where:

- S = sensitivity (m.T^{-1})
- d_0 = static gap
- C_0 = static capacitance
- OSR = over-sampling ratio.

Using the sensitivities and zero deflection capacitances derived above, $d_0 = 1.4 \mu\text{m}$, an OSR of 128, $V_{ref} = 5 \text{ V}$, and $kT = 3.6 \times 10^{-21} \text{ V}^2\text{F}$, the amplitude of the magnetic field for a 6dB SNR is:

$$|B_{\perp}| \approx 21 \text{ nT}$$

The change in capacitance of a xylophone magnetometer as a function of magnetic field has been shown [12] to be:

$$\frac{\partial C}{\partial B_1} \approx \frac{-S}{d_0} C_0 \quad (19)$$

This corresponds to:

$$\frac{\Delta C}{\Delta B_1} = -2.6 \times 10^{-5} \text{ fF.nT}^{-1} \text{ for CMOS devices}$$

and,

$$\frac{\Delta C}{\Delta B_1} = -2.4 \times 10^{-5} \text{ fF.nT}^{-1} \text{ for SOS devices.}$$

For CMOS devices, a field of 21 nT corresponds (using $\Delta Q = V\Delta C$) to a minimum detectable charge of 2.7×10^{-18} Coulombs, or 16 electrons (1 electron = 1.6×10^{-19} C). Furthermore, this method implies that the theoretical minimum detectable magnetic field is about 1.2 nT (field due to charge from a single electron).

Inspection of (6) suggests that doubling *OSR* decreases the minimum detectable field by ~30%. Increasing *OSR* by a factor of 16, for example, reduces the minimum detectable field to 5.1 nT and increases the sampling frequency to 96 MHz. Increasing the sampling rate, however, affects the noise analysis if the bandwidth of the amplifier used in [12] is less than the bandwidth of the sampling network.

In practice, the minimum detectable field will also be limited by the ratio of the dynamic range of the analog output to the analog voltage that corresponds to the minimum detectable field, and by the resolution of the device used to measure the analog voltage. It should be noted that a sensor with a digital output does not have this limitation.

In general, the feasibility of increasing the over-sampling ratio should be investigated. In addition, a more complete analysis should include noise contributions other than thermal noise.

Among the many optical detection schemes have been implemented to detect the displacement of MEMS components, the most common are the optical lever and interferometry. The optical lever [13] is simpler to implement since it does not require the positioning of the input and output beams normal to the reflecting surface. However the resolution is typically limited to approximately $10^{-2} \text{ nm}/\sqrt{\text{Hz}}$. Fiber optic interferometers [14], based on the interference of light between the cleaved end of a fiber and the MEMS device, generally have resolutions of the order of $10^{-3} \text{ nm}/\sqrt{\text{Hz}}$. State-of-the-art optical interferometers using transparent substrates have demonstrated

sensitivities of $6 \times 10^{-5} \text{ nm}/\sqrt{\text{Hz}}$ with microcavities [15] and $2 \times 10^{-5} \text{ nm}/\sqrt{\text{Hz}}$ with diffraction elements [16].

It is expected that the sensitivity of an easily implemented interferometric scheme will be of the order of $10^{-4} \text{ nm}/\sqrt{\text{Hz}}$. With a detection bandwidth of 1 Hz this corresponds to a minimum displacement of 10^{-4} nm . With the sensitivities derived in Section 3, the resultant minimum magnetic field expected to be detected with a $400 \times 19 \mu\text{m}$ xylophone bar magnetometer manufactured in either CMOS or SOS technology is approximately 0.025 nT.

Using a detection bandwidth of 1 kHz, as applicable in rotating platforms, the corresponding minimum displacement is of the order of $3 \times 10^{-3} \text{ nm}$ and the minimum detectable magnetic field is approximately 0.8 nT.

It is anticipated that a working optical interferometric detection scheme will be easier to implement using, at least in the first instance, a hybrid approach and the transparent substrate of SOS technology. The transparent substrate will be a pre-requisite for a truly integrated solution.

In parallel with this study the DARPA-sponsored Application-Specific Integrated MEMS Process Service (ASIMPS) Alpha-users course was attended and a CMOS-based magnetometer was designed. A photograph of a released structure, as delivered from CMU, is shown in figure 32. At the time of writing, it had not been possible to obtain any vibrational characteristics from the structure.

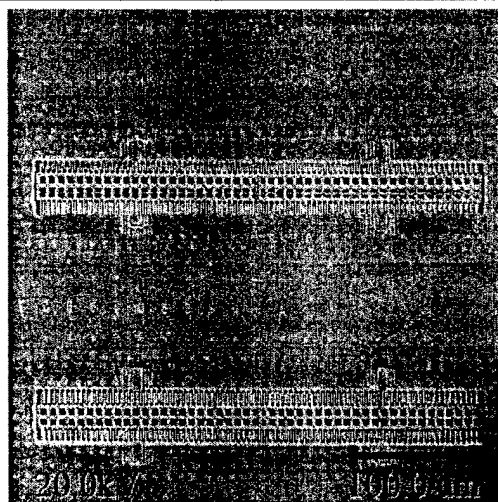


Figure 32 SEM photograph of released CMOS-MEMS xylophone bar magnetometers

5. ARL(Aberdeen)

Some polysilicon MUMPs device structures, including xylophones, cantilevers, and diaphragms, were selected for shock testing, diced into 5 x 5 mm chips, released, and mounted and bonded into 40-pin dual-in-line ceramic packages. An empty such package was fitted with a sapphire window and subjected to shock testing to verify structural survivability. The package was placed in an aluminum housing and encapsulated in a clear potting material. A "window" was fabricated in the top surface by milling out a small patch and refilling by hand pouring a thin layer of epoxy. This technique allows for the optical inspection and characterization of the sensor die without having to release them from the epoxy. The packages were shock tested from 1,000 to 40,000 g's , 0.5 to 0.1ms duration and survived all shocks in this range. Therefore, the device packages were fitted with sapphire windows were shock tested in two orientations up to 30 Kg's. All of the magnetometer elements survived the shock testing. However, it was observed that a few of the magnetometer elements became stuck to the capacitor plates as a result of the shock testing. It was found that the stuck elements could be released by subjecting them to a large Lorentz force with a strong magnet.

The anticipated increase in shock testing did not materialize because of problems in developing reliable eutectic die attach and vacuum packaging technologies. Work at ARL/WMRD therefore concentrated on increasing the applicability of MEMS-based magnetometers in projectile applications.

The major objective of the contract was to develop a MEMS-based magnetometer for use as an orientation (roll rate) sensor on projectiles. As the program progressed, it became obvious that the class of sensitive miniature magnetometers being developed would find other important applications in smart projectiles and bullets, and a particular utilization as a compass or heading device. Given the recent Army/DARPA MOA for Future Combat System (FCS) where mature technologies must be demonstrated for insertion into new weapon systems, this program could be of direct application. The new munition concepts will most likely rely on higher performance MEMS, and a MEMS-based magnetometer could be an important part of that solution.

Historically, the use of magnetometers (as compasses) to measure the direction of travel with respect to the local Earth's magnetic field and to aid inertial measurements units (IMU's) for guidance and navigation have been restricted to wing-stabilized platforms. Since most bullets and/or projectiles roll, even those that are fin-stabilized, classical strapdown IMUs, configured from a constellation of accelerometers and angular rate sensors, will suffer from large inaccuracies over long flight times if not aided. Conventional angular rate sensors have extreme difficulty with scale factor and drift errors on rolling airframes. These errors are due to attitude error buildup in roll, which cross-couples pitch plane dynamics into the yaw plane. In addition, MEMS-based angular rate sensors are at an early stage of development and can be dramatically improved in performance if aided by additional sensors.

A miniature magnetometer mounted on a rolling bullet would serve to significantly increase the IMU accuracy. A recent discovery at ARL/WMRD entitled MAGnetic-SONDE (MAGSONDE) [17] – *ARL patent pending* - is the theoretical basis for this novel augmentation of an IMU on a spinning body containing rate sensors and magnetic sensors. MAGSONDE has been designed for use in continuously rolling airframes for estimation of in-flight angular orientation with respect to the Earth's magnetic field. The MAGSONDE is comprised of both a magnetic sensor and a methodology that determines orientation from sensor phase measurements. Importantly, sensor scale factor and gain variations will not affect MAGSONDE performance.

Although devices responsive to Earth's magnetic field have long been used for heading estimation, MAGSONDE is a new and unique technology. It differs from all other known systems giving orientations with respect to a magnetic field in that those systems use one or more of four basic measurements to determine orientations: 1) field strength along a sensor axes; 2) relative field strength along multiple sensor axes; 3) rate of change of field strength along a sensor axis; and, 4) relative rates of change along sensor axis. In every case, analysis of the measurements is premised on some evaluation of a component of the magnetic field along a sensor axis and requires prior knowledge of the field and/or accurate sensor gain calibration. Making angular measurements using MAGSONDE requires only the magnetic sensor(s) to identify the times at which there is no magnetic field along the sensor axis since MAGSONDE determines orientation from relative phase information in the sensor outputs and is amplitude independent. This feature is important for several reasons: 1) No knowledge of the field strength is required, 2) manufacturing tolerances of scale factor and/or gain variations, which are the bane of many inertial sensors, have no effect on MAGSONDE performance, and 3) only scalar operations are required for the angular measurements.

MAGSONDE could be combined with additional field related data sources to yield : Projectile Orientation in Navigation Terms (POINTER) [18] - *ARL patent pending* - such that direct measurement of the angles in a dual-field environment allows a derived inertial orientation, eliminating integration of the rate sensor data which is impracticable over long periods of flight time on spinning bodies. Examples of additional fields are sunlight, gravity, AGPS RF fields, passive radiometry, millimeter wave radar, and ground-based and flight body-based RF telemetry fields. To make this concept work the MAGSONDE application requires the development of miniature, low-cost, bias-free, MEMS-based magnetometers.

Measurements of the angle between the Earth's magnetic field and a projectile, as illustrated in figure 33, can be used to track its angular motion. On a spinning projectile, the orientation of the sensors is continuously changing with respect to the field, unless the spin axis is parallel to the field. In this case the measurement can be made from phase information in the signals from appropriately located magnetometers. Roll rate with respect to the magnetic field also can be obtained. MAGSONDE consists of both the magnetic sensor and the data reduction methodology that leads to this measurement capability.

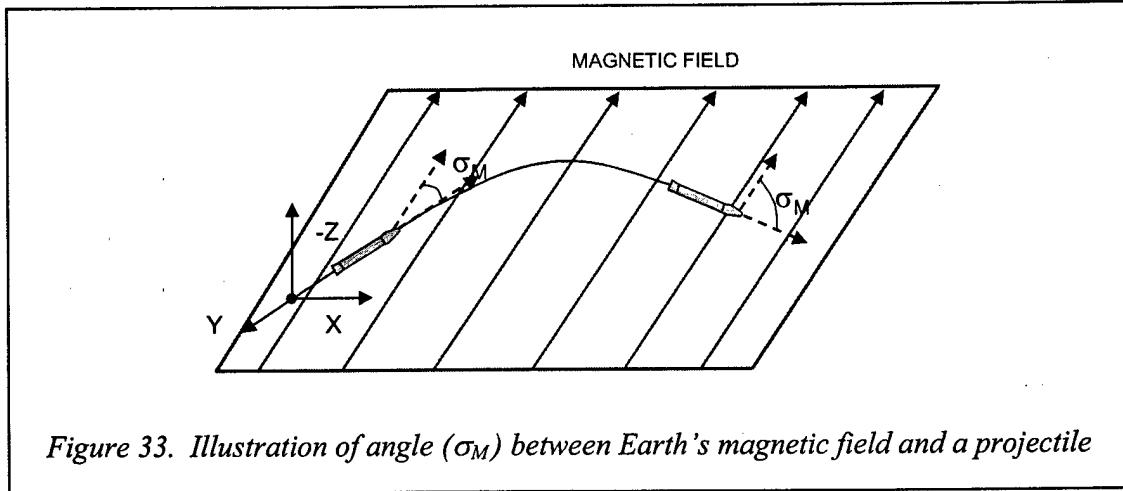


Figure 33. Illustration of angle (σ_M) between Earth's magnetic field and a projectile

The sensor output (O_S), illustrated in figure 34 for two sensors with different orientations, depends on the strength of the magnetic field ($|M|$), the projectile angle in that field (σ_M), the angle of the sensor with respect to the spin axis (λ_S), the roll orientation of the projectile (ϕ_S) and the sensor gain (G_S), according to the equation:

$$O_S = (G_S)|M|[\cos(\lambda_S)\cos(\sigma_M) + \sin(\lambda_S)\sin(\sigma_M)\sin(\phi_S)] \quad (20)$$

Solving for ϕ_S at the zero crossings gives the projectile roll angles at which the respective sensors are orthogonal to the magnetic field. These angles are a function of the sensors' orientations on the projectile and the projectile's orientation in the field, as illustrated in figure 35, and as expressed in the following equation:

$$\phi_S = \sin^{-1} \left[\frac{-\cos(\lambda_S)\cos(\sigma_M)}{\sin(\lambda_S)\sin(\sigma_M)} \right] \quad (21)$$

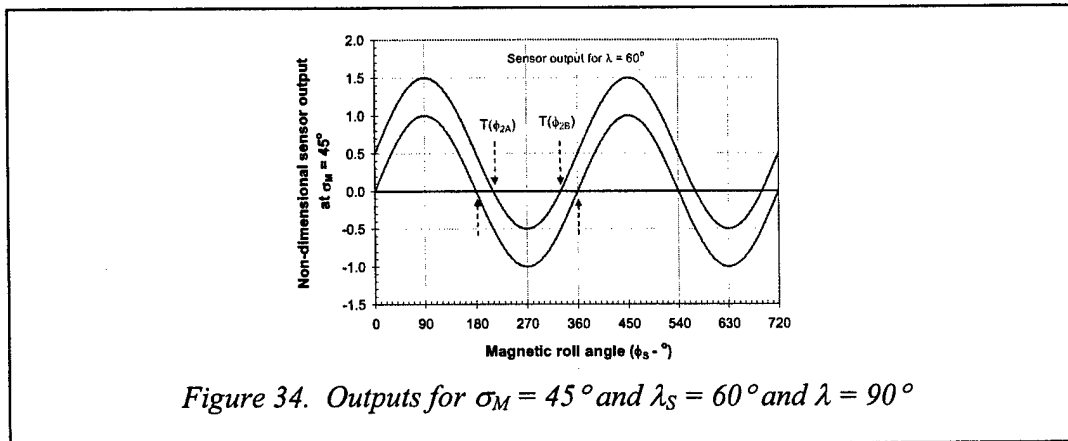
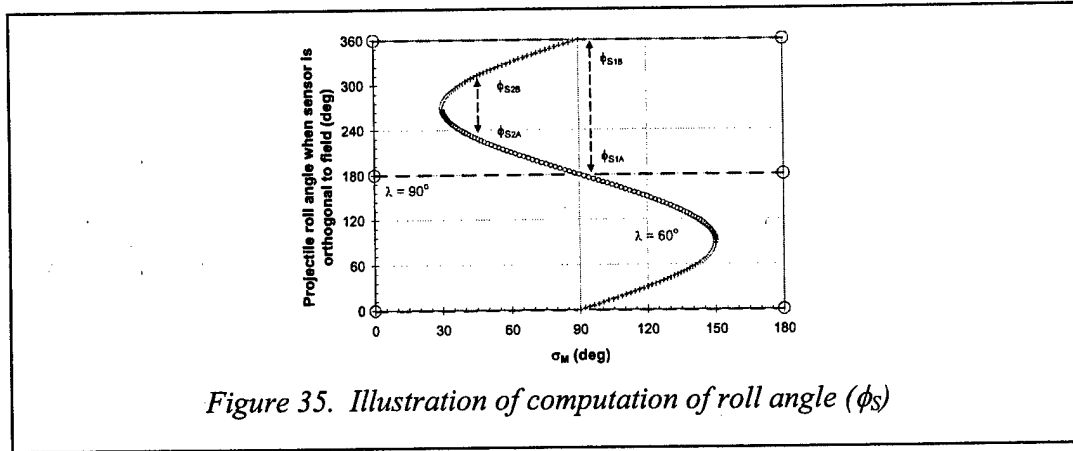


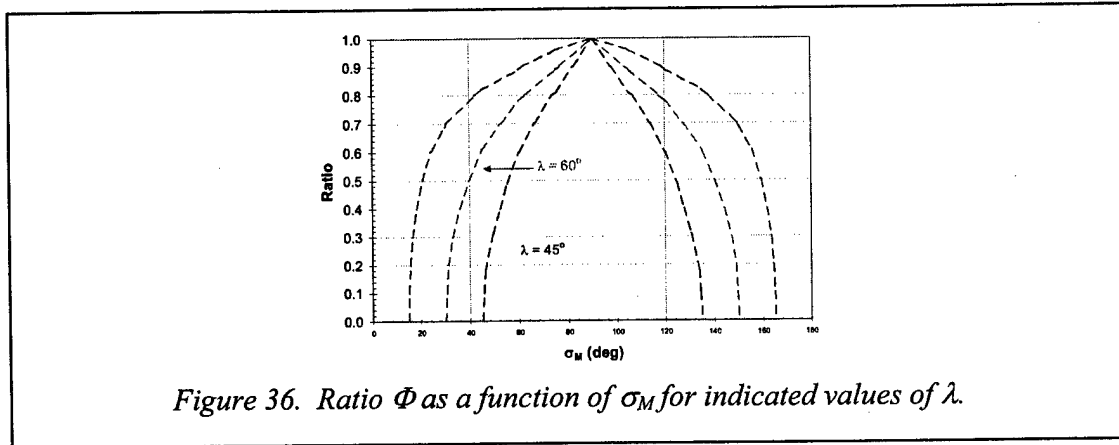
Figure 34. Outputs for $\sigma_M = 45^\circ$ and $\lambda_S = 60^\circ$ and $\lambda = 90^\circ$



The ratio (Φ) of the spacing of these crossings for two sensors with tilt angles that are unequal and non-supplementary is a discriminant of the projectile's orientation in the field:

$$\Phi = \frac{|\phi_{S_{2B}} - \phi_{S_{2A}}|}{|\phi_{S_{1B}} - \phi_{S_{1A}}|} \quad (22)$$

This is illustrated in figure 36. The ambiguity arising from the symmetry of this ratio about $\sigma_M = 0$ is easily resolved by checking the parity of the field along S_1 when S_2 is orthogonal to the field.



The in-flight data will not give sensor roll angles at zero crossings directly but the times at which these crossings occur, as illustrated in figure 34. These times will be used to estimate the ratio:

$$\overline{\Phi} = \left| \frac{T(\phi_{S_{2B}}) - T(\phi_{S_{2A}})}{T(\phi_{S_{1B}}) - T(\phi_{S_{1A}})} \right| \quad (23)$$

If for four consecutive zero crossings (i.e. a roll cycle), the roll rate and projectile angle in the field, σ_M , are constant, the ratio computed from crossing times is equivalent to that computed from roll angles. Though these constraints are seldom completely true in practical flight, the estimation errors are usually small for reasonably stable trajectories.

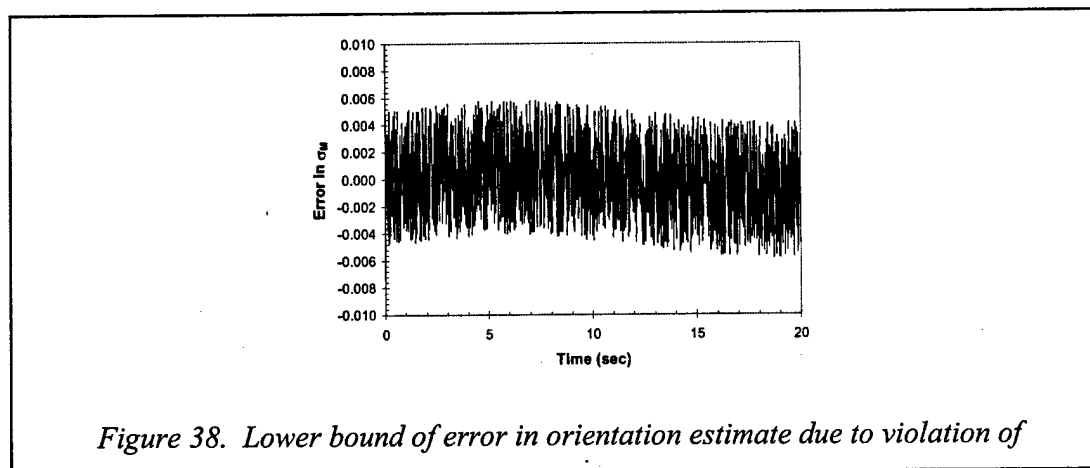
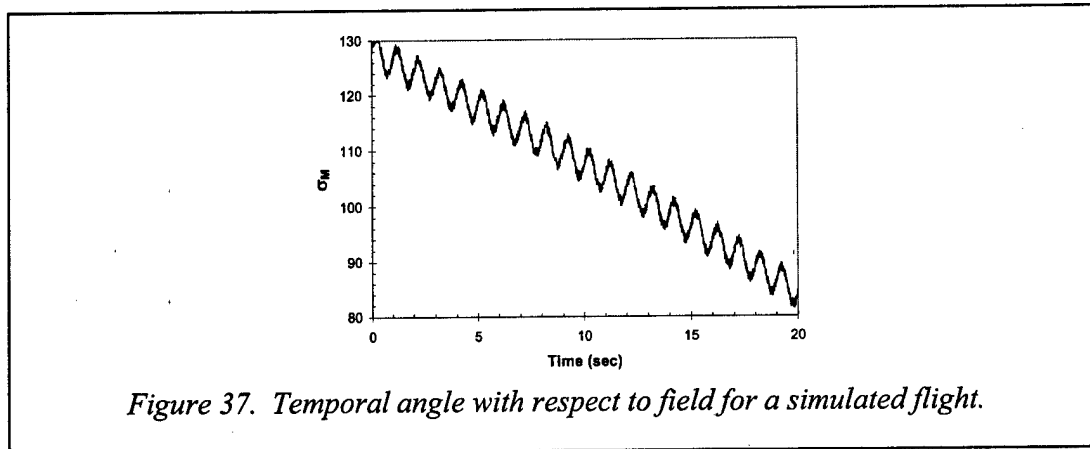
The roll rate is estimated by numerical differentiation of the calibrated crossing positions using the measured crossing times. When σ_M is near 90° and/or the pitch and yaw rates are low compared to the body spin rate, the magnetic roll rate and body spin rate are equivalent.

If the projectile's spin axis is colinear with the magnetic vector (i.e. σ_M is either 0 or 180°), the field strength along the sensor axis is the same throughout a roll cycle and the projectile's magnetic heading can be determined with a parity check. For other projectile headings relative to the field, when $\lambda \neq 90^\circ$, the ratio Φ can only be computed when $(90 - \lambda) \leq \sigma_M \leq (90 + \lambda)$. This bound arises from the existence criterion for a solution to the equation of the roll angle at which the sensor will be orthogonal to the field of:

$$\left| \frac{\cos(\lambda_s)\cos(\sigma_M)}{\sin(\lambda_s)\sin(\sigma_M)} \right| \leq 1 \quad (24)$$

Though this requirement defines a range of magnetic aspect angles for which the ratio can be estimated, this limitation usually can be avoided by either an appropriate choice of launcher aiming or the use of multiple sensors. When this is not possible, it is important to note that this limitation would probably only apply to a portion of the trajectory of many projectiles.

Although the Earth's magnetic field varies both with location and time, these variations are regular and known. Moreover, the variations over the length and duration of a projectile trajectory are typically negligible, excluding local anomalies. Thus, given knowledge of the flight location, the magnetic field near the Earth's surface can be obtained from geodetic survey data, computer models, or direct measurement. Simulated trajectory data, shown in figure 37 for a 6-inch diameter, spin-stabilized artillery round at the Transonic Range at Aberdeen Proving Ground, is then used to estimate the nominal anticipated magnetic heading history. The corresponding lower bound of error in orientation estimate due the violation of constraints outlined above is given in figure 38.



In summary, MAGSONDE determines the orientation from the relative phase information in the sensor outputs and is independent of the magnetic field strength. This feature is important for several reasons;

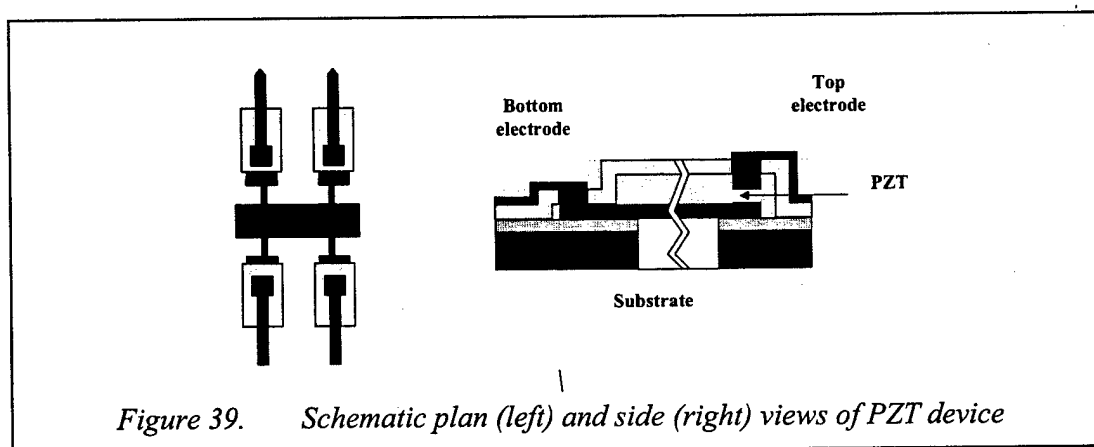
1. No knowledge of the field strength is required;
2. Manufacturing tolerances on scale factor and/or gain variations have no effect on MAGSONDE performance; and,
3. Only scalar arithmetic operations are required for the computation of angular orientations.

In order to implement these concepts in a practicable manner, one requires a sensor whose output is directly proportional to field strength (i.e. a DC sensor), a fast response, and a wide dynamic range. The sensor also has to be small and rugged enough to be mounted on a projectile. This suggests the use of MEMS-based magnetometers in general and the JHU/APL xylophone magnetometer in particular.

6. ARL(Adelphi)

At the start of the contract more than 50 batches of the PZT solutions had been prepared and spun coated on 65 substrates. PZT films (0.25 to 2.0 μm thick) were crystallized using the ARL developed rapid thermal annealing procedure. Remnant polarization P_r ($\mu\text{C}/\text{cm}^2$) and coercive field E_c (kV/cm) were measured to verify the reproducibility of the piezoelectric characteristics of the films. The average measured P_r and E_c values were 20 $\mu\text{C}/\text{cm}^2$ and 72 kV/cm, respectively. The thickness uniformity variation was found to be $\pm 2\%$ across a 4-inch substrate.

A prototype magnetometer, designed for process development rather than operational performance, was designed and is shown schematically in figure 39.



The process steps include:

- a. sol-gel deposit PZT on Si/SiO₂/Pt substrate;
- b. sputter the top Pt electrode;
- c. photolithography define the xylophone structure, ion mill the top Pt, dry etching the PZT, and ion mill the bottom Pt;
- d. selectively expose bottom Pt at contact;
- e. deposit PECVD oxide and open up contact vias for top and bottom electrodes;
- f. deposit and lift-off contact metallization; and,
- g. deep RIE etch substrate and oxide from beneath the xylophone.

An SEM micrograph of a xylophone structure that had completed all the process steps with the exception of final substrate release, is shown in figure 40.

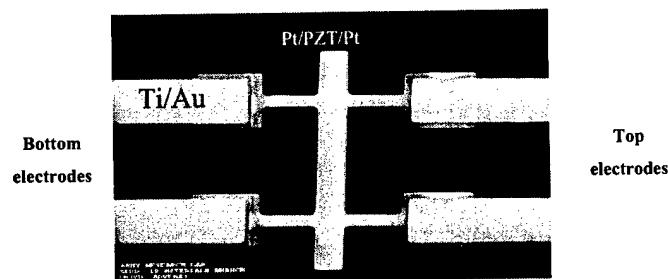


Figure 40. SEM of partly processed Pt/PZT/Pt xylophone structure

Progress on the final release was hampered by problems with the deep reactive ion etch system. However, work continued to develop the process to minimize the residual stress in the Pt/PZT/Pt structure and thus allow the release of an undistorted xylophone bar. In these studies, different layer sequences were deposited on 3" silicon wafers and stress measurements were made using a Tencor FLX-2908 before and after adding each of the layers as well as during and after annealing. In the case of multilayer films, the total thickness of all layers at the given process step was considered. Negative values for stress indicated a compressive stress and positive ones a tensile stress. PECVD oxide and nitride dielectrics were deposited at 250°C and rapid thermal annealed (RTA) annealed at 750°C for 60 sec in nitrogen. Top and bottom metal electrode layers were sputter deposited and either RTA annealed at 700°C for 60 sec or furnace annealed to 700°C (ramped at 15°C/min) under nitrogen. PZT films (250 nm, 500 nm, 1000 nm) were spin coated (ref 6) and the residual stress was measured after crystallization.

The deposition of the bottom electrode layer (20nm Ta/170 nm Pt) onto either dielectric layer did not significantly change the residual stress levels. However, after RTA annealing at 700°C for 60 seconds, the residual stress became tensile at levels of 1070 ± 70 MPa. This is illustrated in figure 41. This effect was examined in more detail by performing an RTA anneal at 750°C after the dielectric deposition and before the electrode deposition. The result of the combined process is illustrated in figure 42 for various thickness of dielectric layer. It can be seen that the results from the oxide layers are very consistent. The RTA annealing after oxide deposition changes a compressive stress of -430 ± 50 MPa to a tensile stress of $+50 \pm 50$ MPa. The stress then reverts to compressive after deposition of the bottom electrode, and then becomes tensile upon RTA annealing of the stack. The residual stress decreases with increasing oxide thickness and varies from 200 to 500 MPa – levels significantly lower than that shown in figure 41. The behavior of the nitride-coated samples was much more varied and resulted in residual tensile stresses in excess of 100 MPa. It is to be noted that the adhesion of the subsequently deposited PZT improved significantly following annealing.

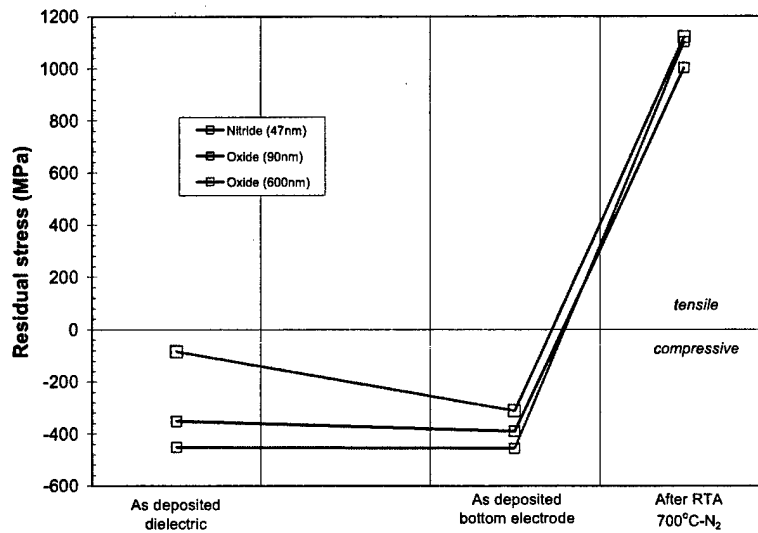


Figure 41 Residual stress after RTA annealing of combined as-deposited bottom dielectric and electrode layers

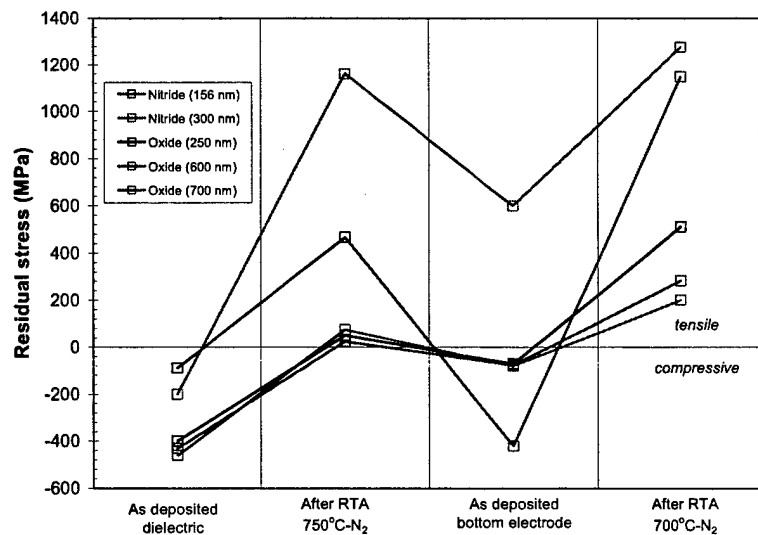
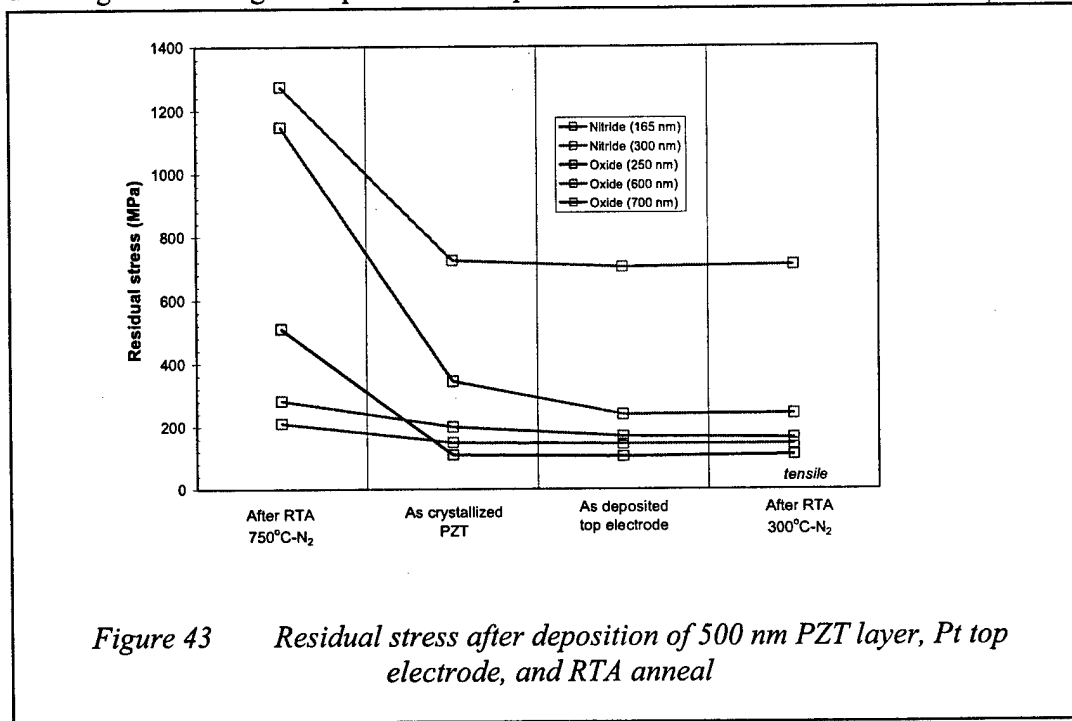


Figure 42 Residual stress after RTA annealing of separate as-deposited bottom dielectric and electrode layers

The effect on residual stress of the subsequent deposition of a 500 nm PZT layer and a Pt top electrode layer, followed by an RTA anneal at 300°C for 60 seconds in N₂, is illustrated in figure 43. In each case, the deposition of the PZT (including the crystallization process) reduces the residual stress to levels that remain essentially unchanged following the top electrode deposition and RTA anneal.



The effect of PZT layer thickness was studied using substrates coated with 600 nm thick PECVD oxide layers and the standard bottom electrode. The general behavior illustrated in figure 43 was observed with the final increasing slightly with PZT thickness. For example, the residual stress after recrystallization varied from 183 MPa for a 250 nm thick PZT layer to 257 MPa for a 1000 nm thick PZT layer. In each case, the residual stress reduced by approximately 70 MPa following the top Pt metallization deposition and 300°C RTA anneal. The final residual stress level of 140±25 MPa tensile is to be compared with a residual stress level of approximately 10 MPa compressive for polysilicon layers. Further studies were undertaken on examining the development of residual stress during the deposition and RTA annealing of multilayers of PZT. A description of the treatments according to the layers is given in Table 2. The stress here was based on the entire thickness of the layer(s). As the layers accumulated, the stress values had less variation and normalized to a tensile value of 175 MPa. Measured negative values for stress indicate a compressive stress and positive ones a tensile stress.

The calculated residual stress of each individual layer is given in Table 3. The as-deposited condition of the SiO₂, top and bottom Pt layers were compressive but changed to the tensile after annealing. The PZT layers varied between 113-148 MPa depending on thickness.

Layer	Avg. Stress (Mpa)	St. Dev. (δ) \pm
SiO ₂	-341	7
RTA SiO ₂ (700°C/60 sec in N ₂)	47	7
Ta/Pt bottom electrode	-23	14
RTA Ta/Pt (700°C/60 sec)	219	6
0.22 μ m PZT	204	7
0.44 μ m PZT	196	9
0.66 μ m PZT	181	14
0.88 μ m PZT	165	18
Pt top electrode	163	4
RTA Pt (350°C/120 sec)	175	6

Table 2. Total accumulated successive stress in piezoelectric multilayer stack.

Layer	Avg. Stress (Mpa)	St. Dev. (δ) \pm
SiO ₂	-341	7
RTA SiO ₂ (700°C/60 sec in N ₂)	47	7
Ta/Pt bottom electrode	-284	14
RTA Ta/Pt (700°C/60 sec)	858	6
0.22 μ m PZT	144	7
0.44 μ m PZT	148	9
0.66 μ m PZT	132	14
0.88 μ m PZT	113	18
Pt top electrode	-113	26
RTA Pt (350°C/120 sec)	-15	37

Table 3. Calculated residual stress of each individual layer in piezoelectric multilayer stack during deposition.

Individual layers were then removed starting from the top of the stack. The measured stress was based on the radius of curvature of the wafer before and after the specific layer removal. Removal of the layers was accomplished by ion milling for the Pt layers, and wet chemical etching for the PZT layers. The results are summarized in Table 4, together with details of the etching steps. The stress values of the removed layers (Table 4) were compared with those of the individual layers (Table 3). The greatest

residual stress was found to be in the in the bottom electrode (518 MPa) after the PZT was removed had the largest difference.

Etch method	Etched layer thickness (Å)	Avg. Stress (Mpa)	St. Dev. (δ)±
Ion milling	1700 top Pt + ~740 PZT	-9	9
Wet etch	3500-6800 PZT	183	19
Ion milling	1900 Ta/Pt + ~900 SiO ₂	518	31

Table 4 Stress due to etched layers.

Advances in process development enabled the release of xylophone bar test structures from the front side of the wafer rather than from the back side. Holes were opened up in the oxide surrounding the xylophone structures and the silicon was removed by use of a 40-μm deep "isotropic" etch in the DRIE system. This resulted in fully released and suspended PZT xylophone bar magnetometer structures as shown in figure 44. The isotropic release process using a SF₆ plasma performed well and did not leave any residue on the top metallization. The xylophone bars have been electrically excited in order to prove piezoelectric actuation within the structure and to locate the fundamental resonance frequencies of the bars.

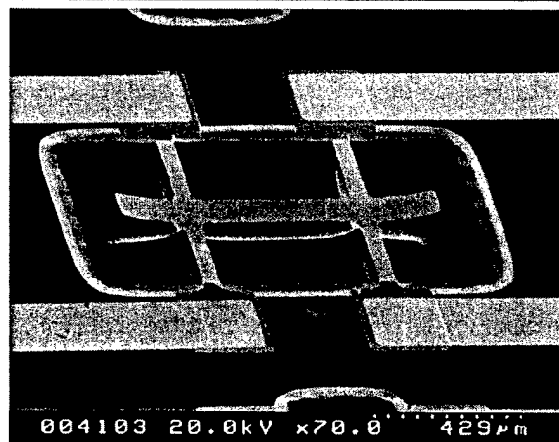


Figure 44. Resultant PZT xylophone bar actuator with the ends of the bar bowing out of plane due to the large tensile stresses in the platinum metallization.

Real-time structural dynamics measurements on a nominally 1 x 0.1 mm device were obtained using a laser Doppler vibrometer. The xylophone bar, operating in air, was actuated with a 1 volt input signal applied to the top electrode which produced a piezoelectric response. Results of the three lowest frequency modes observed are shown in figure 45. The resonance frequencies of the torsion mode (figure 45a), sine wave mode (figure 45b), and the trampoline mode (figure 45c) were 14.84 kHz, 16.03 kHz, and 26.47 kHz, respectively.

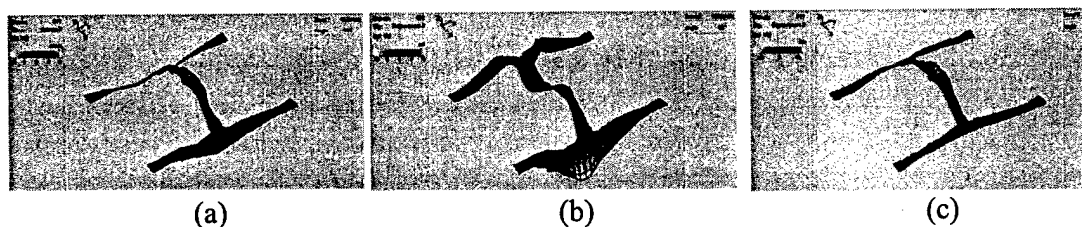


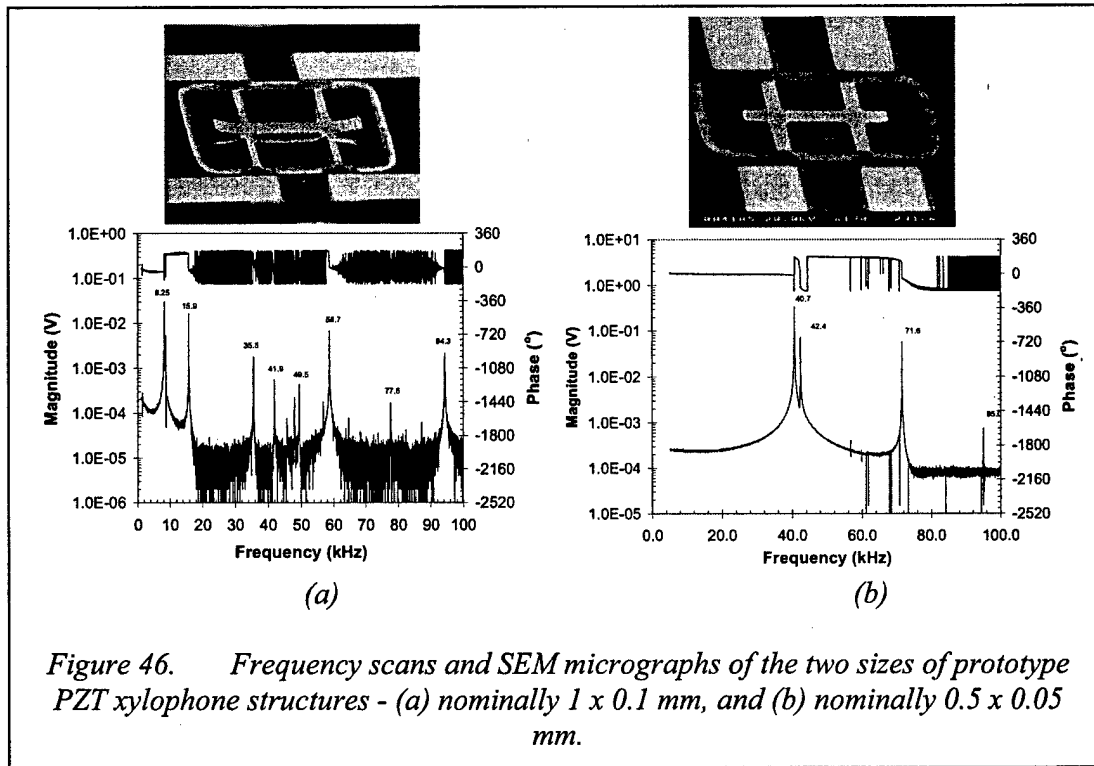
Figure 45 Laser vibrometer scans showing torsion mode(a), sine wave mode (b), and trampoline mode (c) deflections of a xylophone bar test structure.

A part-wafer (approximately 38 x 17 mm in size) containing several operational devices was used in an attempt to characterize their magnetometer performance. Unfortunately, the devices on the wafer had been aligned 45° to the cleavage planes of the substrate and, as a consequence, could not be reduced to a manageable size without endangering the integrity of the released xylophone bars. Therefore, the whole piece was mounted on a large header, which in turn was adapted to fit into the vacuum test fixture.

Initial characterization was undertaken by applying a 1 or 10 mV ac signal across the top electrode and sweeping the frequency from 1 to 100 kHz. The results for a nominally 1 x 0.1 mm and a nominally 0.5 x 0.05 mm device are shown in figures 46(a) and 46(b), respectively. In these figures, the red curves are the magnitude of the beam deflection signals and the blue curves are the phase outputs. Also shown are SEM micrographs of the two types of device. It can be seen that the frequency spectrum is very complex, probably as a result of the non-idealized tether structure.

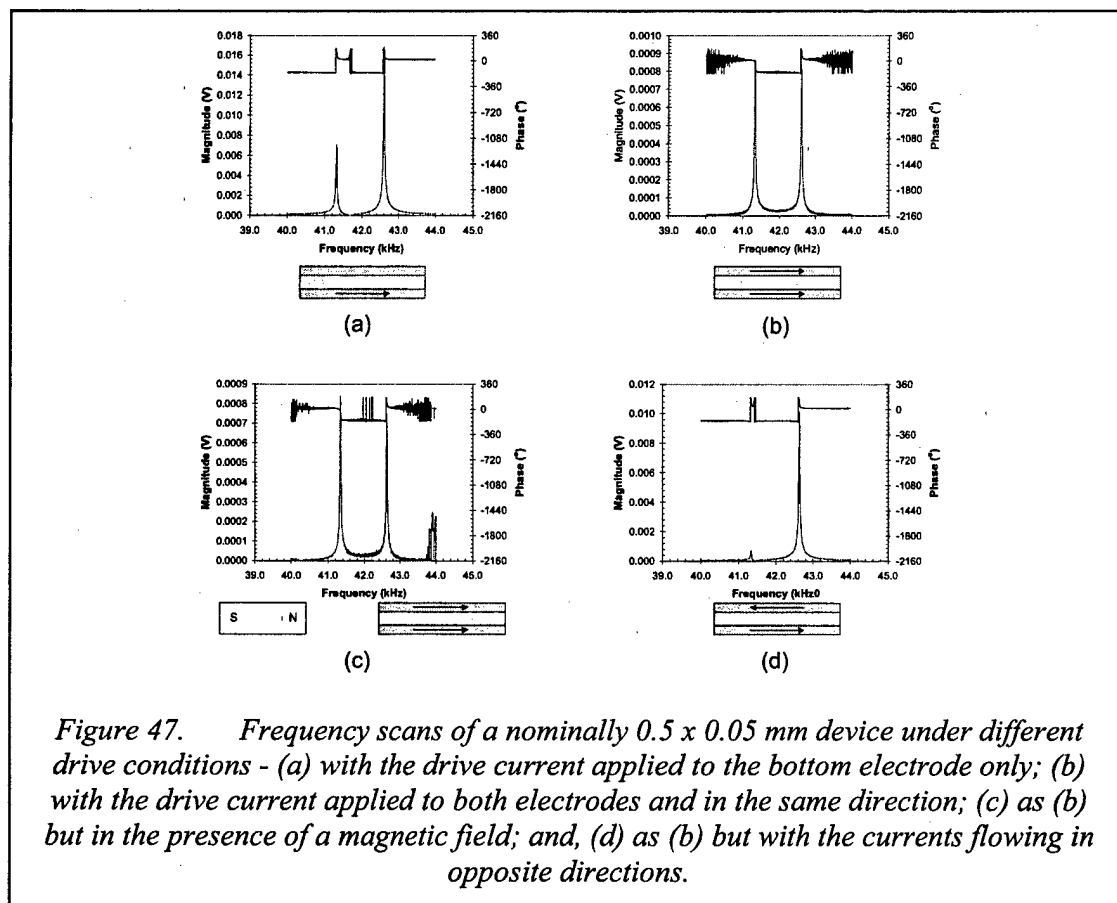
Actual dimensions of the structures were taken from an automated micrometer microscope stage. These dimensions, together with the thickness, density, and Young's modulus of each layer in the structure resulted in expected frequencies of the first torsional mode of 7.34 kHz and 30.13 kHz for the two sizes. This is to be compared with the observed frequencies of 8.31 and 42.4 kHz, respectively. The differences in frequencies observed in the laser vibrometer [figure 45] and in the beam deflection [figure 46(a)] is attributed to the devices coming from different wafers, with the former having unknown thickness of active components. It is also to be noted that significant

differences were observed among the different devices on the same wafer, indicating variation in material characteristics across the wafer.



The region of the lowest frequency mode in all devices tested to date contained two peaks. Figure 47 shows these peaks in some detail in an experiment designed to determine the response of the prototype devices to a magnetic field. This problem was compounded by the fact that the only header available was deep and magnetic and effectively shielded the wafer from any impressed field. Figure 47(a) shows the frequency-scan across the two peaks with a drive current applied to the bottom electrode only. The response could be due to either a Lorentz force between the drive current and the (unknown) magnetic field present, the piezoelectric effect arising from the difference in field across the PZT layer from the voltage drop along the bottom layer, or a mixture of both. Figure 47(b) shows the frequency-scan with the drive current applied to both top and bottom electrodes in the same direction. This configuration should increase the Lorentz contribution and decrease the piezoelectric contribution. It can be seen that the overall magnitude of both peaks is decreased by almost two orders of magnitude, implying that the device is being driven primarily by the piezoelectric response of the PZT, and that the ratio of intensities of the two peaks is different. Figure 47(c) shows the frequency scan with the drive current applied to both top and bottom electrodes in the same direction and in the presence of a strong (~ 1 mT) external magnetic field. There is no significant difference between figures 47(b) and 47(c) - demonstrating the magnetic shielding of the package. (The features in the figure 47(c) scan around 44 kHz are instrument noise). Figure 47(d) shows the frequency-scan with the drive current applied to both top and bottom electrodes in the opposite direction. In this configuration the

Lorentz force component should be significantly reduced (not eliminated because of different resistances of the top and bottom Pt layers) and the piezoelectric component enhanced. It can be seen that the low frequency peak is visibly reduced and the high frequency peak is comparable to that shown in figure 47(a).



Two issues arose out of this fabrication process development. One was the non-planar nature of the resultant released structure, while the other was the low mechanical Q associated with the xylophone bar. The lower than expected Q value was tentatively attributed to an excessive tether width, and design modifications have been incorporated into the mask set to be used in the first prototype device fabrication. The bowing of the released xylophone bar was found to result from the stress gradient in the multilayer stack actuator with specific attention on the high tensile stress of the underlying bottom Ta/Pt metallization layer. The SiO₂ thin film underneath the Pt/PZT/Pt actuator causes the neutral axis of the beam to be located below the bottom Pt metallization. With the large tensile stress of the Pt located above the neutral axis the beam is directed upward away from the substrate surface.

In response to concerns over lower Q and sensitivity values due to the non-planar released beam, several fabrication schemes were initiated to fabricate planar PZT xylophone magnetometers. The most promising result so far was achieved using a high

tensile stress Si_3N_4 layer placed in a SiO_2 sandwich underneath the Pt/PZT/Pt actuator. If the nitride film is placed properly below the neutral axis of the beam, it can offset the highly stressed bottom metallization, thus yielding a stress compensated, planar beam.

The study focused on the fabrication of center clamped resonating bars with a $\sim 500\text{\AA}$ PECVD Si_3N_4 film deposited at different depths within a PECVD SiO_2 sandwich. Table 5 lists the five different fabrication schemes that were investigated as well as the residual stress associated with each film stack as measured after a nitrogen anneal to remove excess trapped hydrogen. The resultant beams revealed a transition from bowing in toward the substrate to bowing away from it.

SiO_2 (\AA)	Si_3N_4 (\AA)	SiO_2 (\AA)	Residual Stress (Mpa)
1000	500	5500	105
2000	500	4500	120
3250	500	3250	50.8
4500	500	2000	13.5
5500	500	1000	-8.5

Table 5. Dielectric structure of center-clamped PZT resonating bars and the residual stress in the dielectric stack after a 700 °C anneal in N_2 .

A mask set for the initial prototype PZT xylophone bar magnetometers, incorporating modifications identified during the initial development phase, was designed. This includes design changes to the tether width so that larger Q values could be realized. In addition, the mask set was meticulously designed to ensure that the tether length could be maintained with specific dimensions after release. Another feature that became apparent during initial development was the difficulty of dicing the wafer without damaging the released structures. The dicing was addressed by designing a deep reactive ion etched (DRIE) trench to be etched in the backside of the silicon wafer prior to the release of the magnetometers. These lines would then serve as crack propagation guides and allow for each individual die to be released without harming the magnetometers.

The first prototype PZT xylophone bar magnetometer devices were fabricated with a multilayer ($\text{SiO}_2/\text{Si}_3\text{N}_4/\text{SiO}_2$) dielectric stack. The goal was to produce a released beam with zero static deflection. These devices were fabricated but still experienced a slight degree of static deflection due to residual stress variability in the multilayer stack. However, the beams could still be tested with laser Doppler vibrometry to measure the electrically excited (1V) resonance modes. Figure 48 illustrates a few of the resonance characteristics for one of the devices operating at atmospheric pressure. The first two resonance modes represent a spurious non-symmetric resonance mode that was

associated with the extremely large static deflections in the beam ends. The fundamental resonance mode was at 69.5 kHz with a 1st harmonic mode at 162.1 kHz.

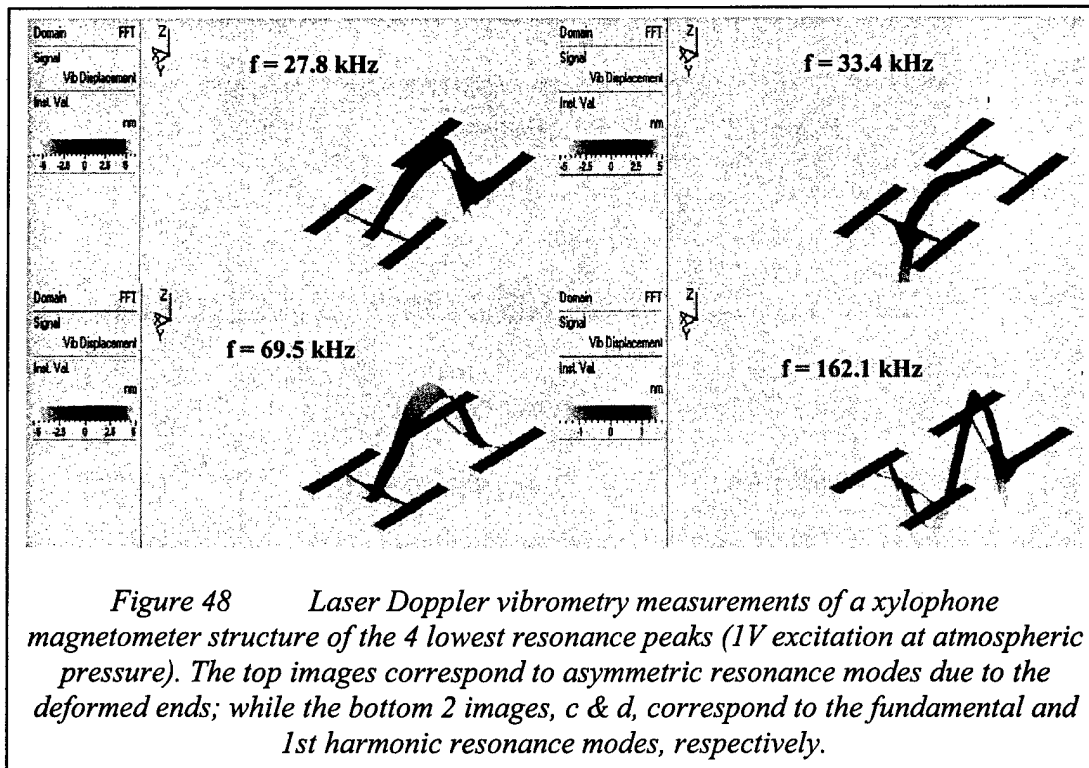
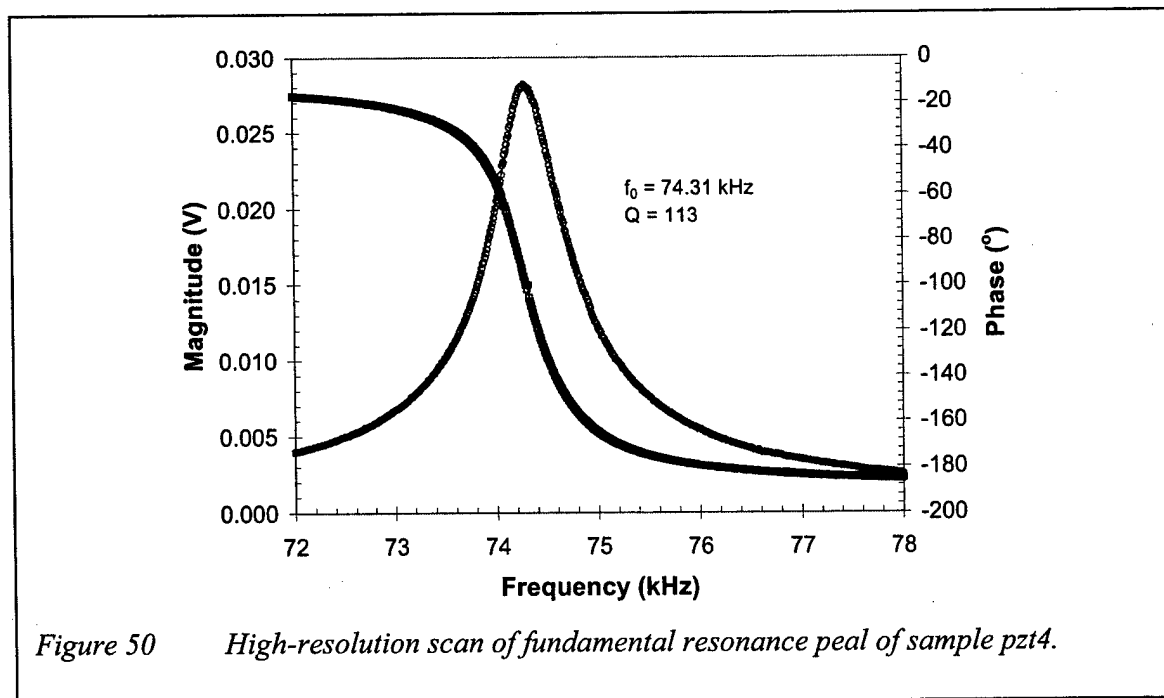
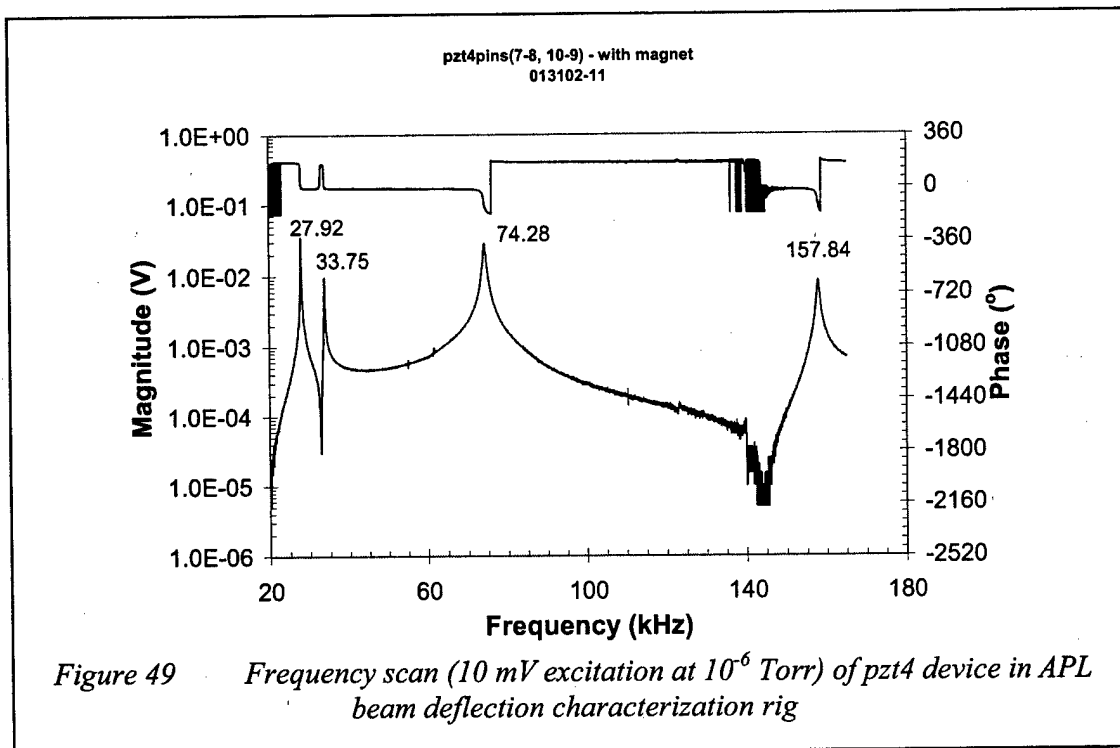


Figure 49 gives the frequency scan of a similar device (designated pzt4) tested in the APL beam deflection rig using a 10 mV excitation. The deflection produced by this excitation, applied with the top and bottom electrodes connected together, was independent of applied magnetic field and in close agreement with the resonance frequencies obtained with the laser vibrometer. The piezoelectric excitation was a result of the different resistances of the top and bottom electrodes producing a net voltage drop across the PZT film.

A high-resolution scan of the fundamental resonance peak of pzt 4 is given in figure 50. The Q-factor is very low at 113. These results demonstrate that current PZT devices, because of their large piezoelectric actuation, are unsuitable for detecting static magnetic fields.



7. CONCLUSIONS

The objective of this project was to develop a sensitive MEMS-based magnetometer for use as an orientation sensor on spinning projectiles. The magnetometer was derived from the JHU/APL resonating xylophone bar with sensitivity linearly proportional to the drive current, mechanical Q at resonance, and the magnetic field. Polysilicon magnetometers demonstrated the size effects expected for such devices. Their sensitivity was limited by the relatively high sheet resistivity that restricted the drive current. A CMOS-based capacitive sense chip was developed, fabricated through MOSIS and tested. This circuit can be used in future designs of magnetometers and other structures such as accelerometers and gyroscopes. PZT-based magnetometers (processed at ARL, Adelphi) were shown, at the current state of development, to be unsuitable for use as vibrating bar magnetometers because of low mechanical quality factors, asymmetric conducting layers, and high residual stress levels. The most promising technology appears to be based on CMOS-MEMS, although more development is required to produce practical devices. Even more recent advances in silicon-on-sapphire (SOS) technologies may make it possible to replace standard capacitive transduction schemes with much more sensitive optical ones. Studies have shown that a MEMS-based magnetometer would have important applications in addition to orientation sensing, particularly when combined with accelerometers and gyroscopes.

8. ACKNOWLEDGMENT/DISCLAIMER

This work was sponsored (in part) by the Air Force Office of Scientific Research, USAF, under grant number F49620-98-1-0500. The views and conclusions contained herein are those of the authors and should not be interpreted as necessarily representing the official policies or endorsements, either expressed or implied, of the Air Force Office of Scientific Research or the U.S. Government.

9. REFERENCES

1. W. P. D'Amico, "Revolutionary technologies for miniature measurement systems - Application to ground testing," 36th Aerospace Sciences Meeting, Reno, 1998 (AIAA 98-0234).
2. T. G. Brown, "Free flight yawsonde test of the M712 Copperhead projectile," BRL-MR-3798, U.S. Army Ballistic Research Laboratory, Aberdeen Proving Ground, MD, 1989.
3. T. E. Harkins and B. S. Davis, "Using giant magnetoresistive radio (GMR) materials as a navigation aid for smart artillery projectiles," ARL-TR-1330, U.S. Army Research Laboratory, Aberdeen Proving Ground, MD 1997.
4. R. B. Givens, J. C. Murphy, R. Osiander, T. J. Kistenmacher, and D. K. Wickenden, "A high sensitivity, wide dynamic range magnetometer designed on a xylophone resonator," Appl. Phys. Lett. **69**, 2755-2757 (1996).

5. Young W.C., *Roark's Formulas for Stress and Strain*, 6th Edition, McGraw-Hill, New York, 1989.
6. D. K. Wickenden, R. B. Givens, R. Osiander, J. L. Champion, D. A. Oursler, J. L. Lamb, and T. J. Kistenmacher, "Heterodyne detection of alternating magnetic fields with a resonating xylophone bar magnetometer," *Appl. Phys. Lett.*, **74**, 1472-1474 (1999).
7. D. Sherman, "An Investigation of MEMS Anchor Design for Optimal Stiffness and Damping," Master's Project, University of California, Berkeley, May 1996.
8. J. L. Lamb, D. K. Wickenden, J. L. Champion, R. B. Givens, R. Osiander, and T. J. Kistenmacher, "Micromachined polysilicon resonating xylophone bar magnetometer: Resonance characteristics," *Mat. Res. Soc., Symp. Proc.* **605**, 211-216 (2000).
9. H. Xie and G. K. Fedder, "A CMOS Z-Axis Capacitive Accelerometer With Comb-Finger Sensing," The 13th Annual International Micro Electro Mechanical Systems Conference Miyazaki, Japan, Jan 23-27, 2000, pp. 496-501.
10. M. Parameswaram, A. M. Robinson, D. L. Blackburn, M. Gaitan, and J. Geist, "Micromachined thermal radiation emitter from a commercial CMOS process," *IEEE Electron Devices Letters*, **12**, 57-59 (1991).
11. C. H. Mastrangelo, J. H.-J. Yeh, and R. S. Muller, "Electrical and optical characteristics of vacuum-sealed polysilicon microlamps," *IEEE Trans. Electron Devices* **39**, 1363 (1992).
12. J. C. Tucker, "MEMS Magnetic Field – Capacitance Relationship and Signal to Noise Ratio," SEE-01-071, JHU/APL (2001).
13. G. Meyer and N. A. Amer, "Novel approach to atomic force microscopy," *Appl. Phys. Lett.* **53**, 1045 (1988).
14. D. Rugar, H. J. Mamin, and P. Guethner, "Improved fiber-optic interferometer for atomic force microscopy," *Appl. Phys. Lett.* **55**, 2588 (1989).
15. T. H. Stievater, W. S. Rabinovch, H. S. Newman, R. Mahon, P. G. Goetz, J. L. Ebel, and D. J. McGee, "Measurement of thermal-mechanical noise in microelectromechanical systems," *Appl. Phys. Lett.* **81**, 1779 (2002).
16. N. A. Hall and F. L. Degertekin, "Integrated optical interferometric detection method for micromachined capacitive acoustic transducers," *Appl. Phys. Lett.* **80**, 3859 (2002).

17. T. Harkins and D. Hepner, "MAGSONDE: a device for making angular measurements on spinning projectiles using magnetic sensors," SPIE Volume **4025**, Acquisition, Tracking, and Pointing, Orlando, FL, (2000).
18. D. Hepner and T. Harkins, "Determining inertial orientation of a spinning body with body-fixed sensors," SPIE Volume **4025**, Acquisition, Tracking, and Pointing, Orlando, FL, (2000).